Quaternary Science Reviews 182 (2018) 1–19

Contents lists available at ScienceDirect

Quaternary Science Reviews

journal homepage: www.elsevier.com/locate/quascirev

Asynchronous glaciations in arid continental climate

Jigjidsurengiin Batbaatar [a, *], Alan R. Gillespie [a, **], David Fink [b], Ari Matmon [c], Toshiyuki Fujioka [b]

[a] Quaternary Research Center, University of Washington, Seattle, WA 98195-1310, USA
[b] Australian Nuclear Science and Technology Organisation, PMB1, Menai, 2234, Australia
[c] The Institute of Earth Sciences, Hebrew University of Jerusalem, Givat Ram, Jerusalem 91904, Israel

ARTICLE INFO

Article history:
Received 11 March 2017
Received in revised form
30 November 2017
Accepted 1 December 2017

Keywords:
Central Asia
Asynchronous glaciation
Sublimation
Pleistocene
Holocene

ABSTRACT

Mountain glaciers at ~26–19 ka, during the global Last Glacial Maximum near the end of the last 10^5 yr glacial cycle, are commonly considered on the basis of dating and field mapping in several well-studied areas to have been the largest of the late Quaternary and to have advanced synchronously from region to region. However, a numerical sensitivity model (Rupper and Roe, 2008) predicts that the fraction of ablation due to melting varies across Central Asia in proportion to the annual precipitation. The equilibrium-line altitude of glaciers across this region likely varies accordingly: in high altitude, cold and arid regions sublimation can ablate most of the ice, whereas glaciers fed by high precipitation cannot ablate completely due to sublimation alone, but extend downhill until higher temperatures there cause them to melt. We have conducted field studies and ^{10}Be dating at five glaciated sites along a precipitation gradient in Mongolia to test the Rupper/Roe model. The sites are located in nearby 1.875 × 1.875° cells of the Rupper/Roe model, each with a different melt fraction, in this little-studied region. The modern environment of the sites ranges from dry subhumid in the north (47.7° N) to arid in the south (45° N). Our findings show that the maximum local advances in the dry subhumid conditions predated the global Last Glacial Maximum and were likely from MIS 3. However, we also found that at ~8–7 ka a cirque glacier in one mountain range of the arid Gobi desert grew to a magnitude comparable to that of the local maximum extent. This Holocene maximum occurred during a regional pluvial period thousands of years after the retreat of the Pleistocene glaciers globally. This asynchronous behavior is not predicted by the prevailing and generally correct presumption that glacier advances are dominantly driven by temperature, although precipitation also plays a role. Our findings are consistent with and support the Rupper/Roe model, which calls for glaciation in arid conditions only at high altitudes of sub-freezing temperatures, where the melt fraction in ablation is low. We expect a heterogeneous pattern of glacial responses to a changing modern climate in cold arid regions; an individual glacier advance should not be necessarily interpreted as evidence of cooling climate.

1. Introduction

Glaciers respond to a number of forcing functions that are active over a wide range of scales from local (e.g., topographic shadowing) to regional or even global. Of these, annual snowfall and summer air temperature are commonly considered to be the most important. If one of these parameters is independently known, glacial records may be useful in reconstructing the other parameter in continental settings where paleoclimate proxy records are scarce. Specifically, the timing and magnitude of local maximum glacial advances have been used to improve the understanding of changes in climate during the past cycle of glaciation (e.g., Gillespie and Molnar, 1995; Porter, 2001; Clark et al., 2009).

The global "Last Glacial Maximum" (LGM) is defined as the period during the latest ~10^5 yr glacial cycle when the global ice volume achieved its maximum. Climate reconstructions based on oxygen-isotope records of marine foraminifera (Hays et al., 1976) placed the timing of the global LGM at ~23–19 ka (Mix et al., 2001). Integrating the high-latitude ice-sheet and mountain-glacier records appeared to strengthen the concept of a synchronous global LGM and also extended its period to ~26–19 ka (Clark et al., 2009).

* Corresponding author.
** Corresponding author.
E-mail addresses: bataa@uw.edu (J. Batbaatar), arg3@uw.edu (A.R. Gillespie).

https://doi.org/10.1016/j.quascirev.2017.12.001
0277-3791/

However, recent evidence from mid-latitude southern hemisphere glacial records (Augustin et al., 2004; Putnam et al., 2013; Rother et al., 2015; Darvill et al., 2016) and continental Asian valley glacier systems (Gillespie et al., 2008; Koppes et al., 2008; Heyman et al., 2011a; Batbaatar and Gillespie, 2016; Gribenski et al., 2016) suggests a more complex behavior than that of synchronized 'global' glaciations, highlighting the often-overlooked importance of regional factors. Such spatial variations in the magnitude of glaciations during a given period were suspected before (Gillespie and Molnar, 1995; Hughes et al., 2013), but with the widespread introduction of *in-situ* cosmogenic surface exposure dating, new quantitative glacial chronologies (e.g., Hughes et al., 2013; Heyman, 2014) have allowed a reliable temporal comparison of maximum mountain glaciations that might not coincide with the timing of the global LGM.

Glacial records from the arid to humid continental environments (Zomer et al., 2008) of Central Asia (Fig. 1) have revealed that the spatial patterns of glacier advances and retreats as well as the timing of the maxima differ from place to place on a scale of a few hundred kilometers. We postulate that the concept of synchronous glaciations may break down in arid environments where glacier mass balance is controlled by different suites of factors than in more humid settings (e.g., Cuffey and Paterson, 2010, pp. 169–173). For example, in arid–dry subhumid parts of the Kyrgyz Tien Shan (locations are shown in Fig. 1) the largest glaciers date from Marine Oxygen-Isotope Stage (MIS) 3 or earlier, and MIS 2 glaciers were restricted to cirques (Koppes et al., 2008; Blomdin et al., 2016). On the other hand, in humid southern Siberia, the largest glaciers dated from MIS 3, and the MIS 2 glaciers were only slightly smaller (Gillespie et al., 2008; Batbaatar and Gillespie, 2016). In parts of the northeastern Tibetan plateau, the largest mountain glaciers occurred earlier than ~100 ka (i.e. prior to MIS 4) and no evidence of MIS 2 glaciation has been found (Heyman et al., 2011a). Numerical glacial modeling (Rupper and Roe, 2008; Rupper et al., 2009), albeit of low spatial resolution (1.875°), suggests that this heterogeneous pattern of glacial response is due to the different sensitivity of glaciers to climate forcing in cold, arid regions, where sublimation accounts for more than 50% of the total ice loss. However, this model (Rupper and Roe, 2008; Rupper et al., 2009) has yet to be validated with field observations.

In this article, we examined the glacial history in five sites in central Mongolia (Fig. 2), with modern environments grading northward from arid to dry subhumid. The sites are distributed across a cluster of five cells of the Rupper and Roe model (2008) (Fig. 3). We selected the sites to be in cold continental climates where melt versus sublimation was predicted to be a significant factor controlling glacier mass balance, and therefore where glaciers and paleoglaciers could be used to test the Rupper/Roe numerical model. According to the Rupper/Roe model, almost all of glacier ice in arid Gichginii is lost via sublimation and in the semiarid Sutai and Ih Bogd ~10–30% of ice is lost via sublimation. In contrast, in dry subhumid Hangai region melting is responsible for more than 40–60% of total ablation (Fig. 3).

In low-precipitation, sub-freezing sublimation regimes, glaciers are restricted to altitudes close to or above the zero isotherm. As snowfall increases above the amount that can be ablated by sublimation, the glacier will advance below the zero isotherm, but not far because melting is much more efficient at ablation than sublimation. Only when the incoming glacier ice plus the local snowfall in the melt zone exceeds ablation will glaciers flow to lower altitudes. This is a mechanism for desynchronizing glacier advances because of their non-linear response to precipitation differences from place to place: in arid regions glaciers may be restricted to cirques, whereas in more humid regions they may advance or retreat. Likewise, glacier advances in a given valley may respond differently in the face of climate change, for the same reasons.

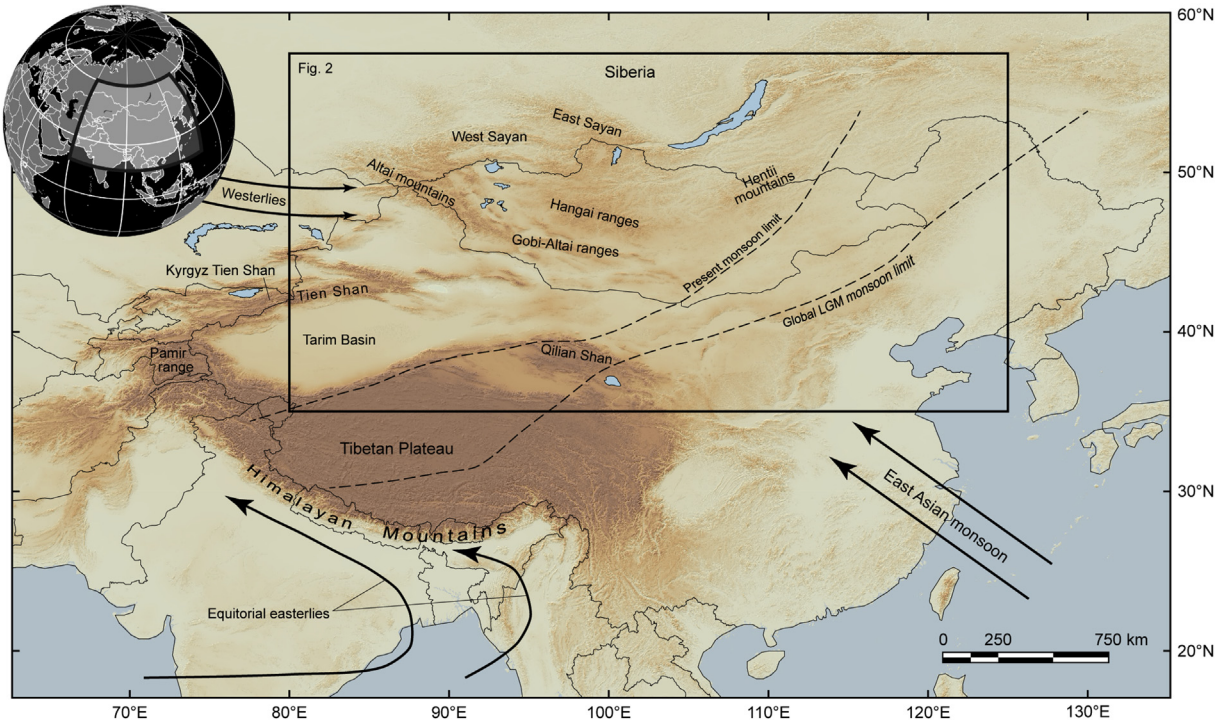

Fig. 1. Geographic location of the Hangai and Gobi-Altai ranges in East and Central Asia. Dashed lines indicate the modern and global LGM limits of East Asian monsoon (Shi, 2002). Solid lines indicate the general direction of major air flows (Benn and Owen, 1998). The black rectangle inset refers to the extent of region shown in Fig. 2.

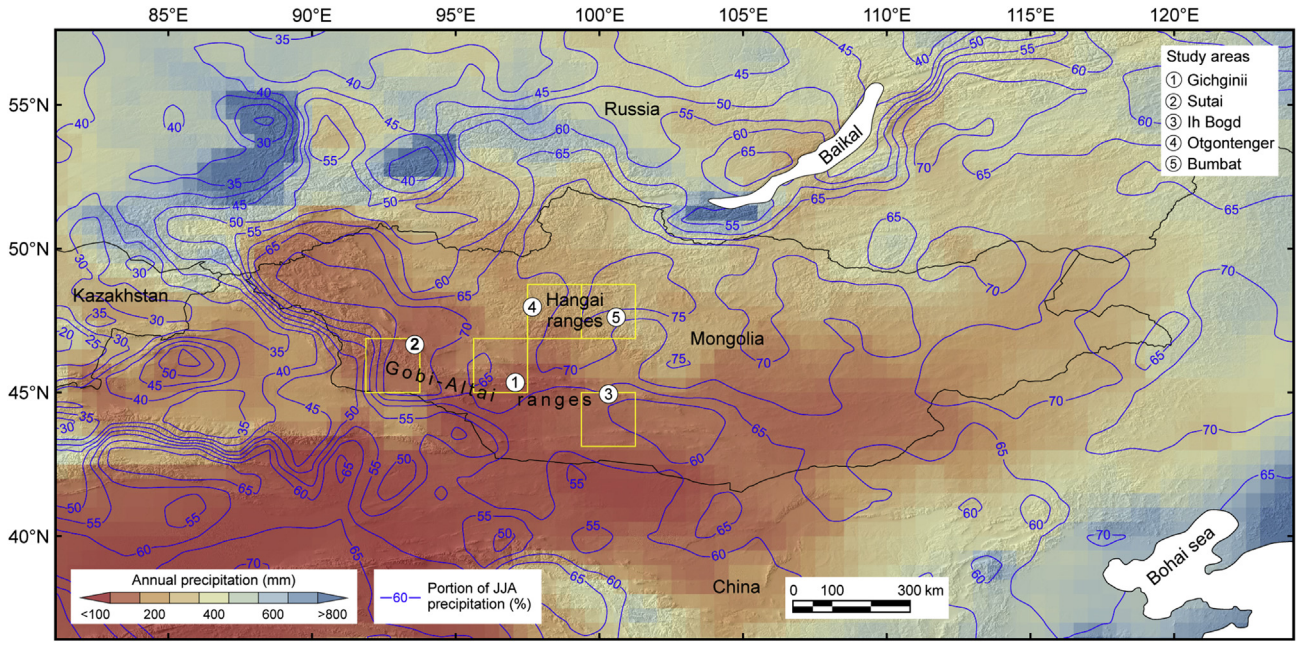

Fig. 2. Modern annual precipitation and the fraction occurring during summer in Mongolia and adjacent areas. The precipitation data are long-term (1981–2010) monthly means (GPCC V7, at 0.5° × 0.5° resolution; Schneider et al., 2016). The yellow rectangles show the 1.875° cells of the Rupper and Roe (2008) model that were occupied by our field study sites. The shaded relief image in the background is constructed from SRTM V3 data (NASA, 2015).

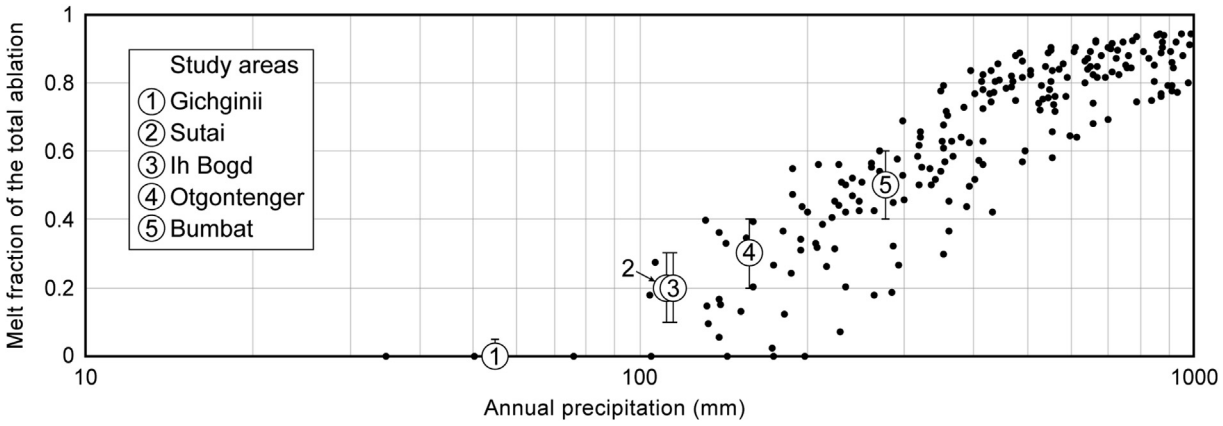

Fig. 3. Modern annual precipitation and modeled melt fraction of the total ablation at the study sites. The precipitation data were from GPCC V7, at 0.5° × 0.5° resolution (Schneider et al., 2016). The melt fraction was modeled and calculated by Rupper and Roe (2008) to 3000 mm yr^{-1}, but only the 10–1000 mm yr^{-1} range is shown here (note the logarithmic scale). The range of melt fractions calculated in the model for a given annual precipitation similar to the study sites is shown by the whiskers.

Both air temperature (T_a) and precipitation decreased during the global LGM in our study area (e.g., Rupper and Koppes, 2010), and the Rupper/Roe model implies that T_a depression alone cannot drive advance of sublimation-dominated glaciers. We test this model implication in the field by seeking evidence of two modes of glacial asynchrony: 1) asynchrony in the timing of maximum glacier extents between sublimation- and melt-dominated regions; 2) asynchrony in the magnitude of glacier extents within the same sensitivity region due to variability of precipitation changes. However, the Rupper/Roe model covers a vast geographic area with a wide range of climatic conditions. Therefore, until more field mapping and dating can be performed the results discussed in this article should be viewed as a preliminary check of the model.

2. Methods

We sampled 59 glacially deposited boulders and one glacially eroded bedrock knob from five sites in four different mountain ranges (Fig. 2) encompassing an area of 15×10^3 km^2. We constructed glacial chronologies in the valleys using ^{10}Be cosmogenic exposure dating (Table 1 and Online Supplements 1 and 2). Nine additional samples from post-glacial strath terraces at Sutai were sampled to determine a minimum age for the glaciers. We also estimated equilibrium-line altitudes (ELAs) for the dated moraines, and using a numerical model (after Rupper and Roe, 2008) examined the climate parameters that influence the glacier ablation. To constrain the local adiabatic lapse rate, we measured summer air temperatures atop the modern ice cap of Sutai. Below, we provide

Table 1
^{10}Be exposure-ages for samples from the Gobi-Altai and Hangai ranges. Ages are ordered by increasing altitude for each site.

Site	Sample identification	Sample description	Maximum diameter (m)	Boulder height (m)	Exposure age (ka)	1σ uncertainty (ka)	
						Internal[a]	External[b]
Gichginii range	*Lateral moraine G2, N 45.4038°, E 97.0704°, 3283–3327 m asl*						
Mönh Mösnii valley	GN-AG-10B	Quartz vein in schist boulder	0.5	0.3	6.9	0.2	0.4
	GN-AG-11	Quartz vein in schist boulder	0.5	0.4	8.1	0.2	0.5
	GN-JB-004	Quartz vein in schist boulder	0.4	0.2	5.3 *	0.3	0.4
	GN-JB-005	Quartz vein in schist boulder	0.5	0.4	7.5	0.3	0.5
	Lateral moraine G3, N 45.4014°, E 97.0701°, 3340–3361 m asl						
	GN-AG-07	Quartz vein in schist boulder	0.5	0.3	1.6	0.1	0.1
	GN-AG-08	Quartz vein in schist boulder	0.4	0.3	3.2	0.1	0.2
	GN-AG-04	Quartz vein in schist boulder	0.4	0.3	0.8 *	0.03	0.1
	GN-AG-05	Quartz vein in schist boulder	0.3	0.3	2.8	0.1	0.2
	GN-AG-06	Quartz vein in schist boulder	0.4	0.3	2.6	0.1	0.2
	Lateral moraine G4, N 45.4013°, E 97.0697°, 3330–3338 m asl						
	GN-JB-001	Quartz vein in schist boulder	0.4	0.3	0.9	0.1	0.1
	GN-JB-002	Quartz vein in schist boulder	0.5	0.4	1.0	0.1	0.1
	GN-JB-003	Quartz vein in schist boulder	0.6	0.4	1.5	0.3	0.3
	GN-AG-01	Quartz vein in schist boulder	0.5	0.4	1.8	0.1	0.1
	GN-AG-02	Quartz vein in schist boulder	0.5	0.2	1.9	0.1	0.1
	GN-AG-03	Quartz vein in schist boulder	0.5	0.3	1.6	0.05	0.1
Sutai range	*End moraine NE1, N 46.6418°, E 93.5710°, 3160 m asl*						
Northeastern slope	DHC-98-12	Quartz vein in schist boulder	2	1	7.3 *	0.3	0.5
	Left-lateral moraine NE2, N 46.6403°, E 93.5648°, 3240–3270 m asl						
	DHC-98-13	Quartz vein in schist boulder	2.5	0.5	26.2	0.8	1.7
	DHC-98-10	Quartz vein in schist boulder	0.8	0.5	22.9	0.7	1.5
	Left-lateral moraine NE4, N 46.6404°, E 93.5660°, 3250 m asl						
	DHC-98-11	Quartz vein in schist boulder	2	0.8	24.9	1.2	1.8
	Recessional (?) left-lateral moraine, N 46.6398°, E 93.5652°, 3265 m asl						
	DHC-98-15	Quartz vein in schist boulder	2.3	0.6	6.7 *	0.2	0.4
Sutai range	*Marginal moraine between ice caps #1 and 2, N 46.6323°, E 93.5688°, 3620 m asl*						
Marginal samples	MOT98-CS-11a	Quartz vein in schist boulder	0.6	0.3	45.0	1.2	2.8
	MOT98-CS-11b	Quartz vein in schist boulder	0.6	0.3	13.2	0.6	0.9
	MOT98-CS-12	Quartz vein in schist boulder	0.5	0.3	24.8	1.6	2.1
	Erratic at the margins of modern ice cap #3, N 46.6052°, E 93.6192°, 3934 m asl						
	SUT-JB-04A	Vein quartz erratic	0.3	0.2	21.3	0.4	1.2
	Erratic at the margins of modern ice cap #3, N 46.6044°, E 93.6194°, 3926 m asl						
	SUT-JB-04B	Vein quartz erratic	0.25	0.1	41.6	1.0	2.5
Sutai range	*Glacially eroded bedrock knob, N 46.5999°, E 93.5487°, 3109 m asl*						
Southwestern slope	MOT98-CS-22	Porphyroblastic schist bedrock	–	–	22.1	0.8	1.5
	Erratic on the bedrock knob, N 46.5999°, E 93.5487°, 3109 m asl						
	MOT98-CS-23	Quartz vein in schist erratic	2	0.8	72.4 *	2.6	4.8
	Recessional moraine (?), N 46.6094°, E 93.5522°, 3180 m asl						
	MOT98-CS-14	Quartz vein in green schist boulder	0.5	0.1	35.6 *	1.8	2.7
	Boulder outside the crest of moraine SW2, N 46.6101°, E 93.5475°, 3189 m asl						
	MOT98-CS-25	Quartz vein in schist boulder	2	1.5	6.0 *	0.2	0.4
	Right-lateral moraine SW2, N 46.6132°, E 93.5503°, 3240–3270 m asl						
	SUT-JB-02A	Quartz vein in schist boulder	0.5	0.3	15.4	0.4	0.9
	SUT-JB-02B	Quartz vein in schist boulder	0.5	0.3	19.8	0.6	1.3
	SUT-JB-02C	Quartz vein in schist boulder	0.3	0.3	13.9	0.4	0.9
	SUT-JB-02D	Quartz vein in schist boulder	2.5	0.6	15.5	0.5	1.0
Ih Bogd range	*Lateral-end moraine IB5, N 44.9564°, E 100.2668°, 3385–3390 m asl*						
Artsan valley	IB-JB-003E	Granitic boulder	1.5	1	16.7	1.2	1.5
	IB-JB-003A	Porphyritic granitic boulder	1	1	7.3 *	0.5	0.6
	IB-JB-003B	Granitic boulder	1.3	1	13.2	1.8	1.9
	IB-JB-003C	Granitic boulder	1	0.5	14.3	0.7	1.1
	IB-JB-003D	Granitic boulder	2	1	13.9	0.9	1.2
	End moraine IB6, N 44.9567°, E 100.2672°, 3402 m asl						
	IB-JB-002	Granitic boulder	2.5	1.5	13.4	0.7	1.0
	Highest lateral-end moraine IB7, N 44.9578°, E100.2675°, 3425 m asl						
	IB-JB-001	Porphyritic granitic boulder	2.5	1	14.4	0.8	1.2
Otgontenger	*End moraine BO1, N 47.6833°, E 97.2067°, 2075 m asl*						
Bogd valley	OT-AG-1	Granitic boulder	1.5	1	22.7	1.2	1.8
	OT-AG-2	Granitic boulder	1.6	1.6	20.2	1.4	1.8
	OT-AG-3	Granitic boulder	2	0.5	23.6	1.3	1.9
Otgontenger	*Right-lateral moraine BI2, N 47.5755°, E 97.6677°, 2580 m asl*						
Bitüüt valley	DHC-98-5	Granitic boulder	1.5	1	31.3	1.0	2.0
	DHC-98-7	Granitic boulder	3	3	82.9 *	2.6	5.3
	DHC-98-8	Granitic boulder	2	0.3	29.9	0.9	1.9
	End moraine, BI8, impounding a lake, N 47.5978°, E 97.6497°, 2725 m asl						
	MOT98-CS-02	Granitic boulder	2	0.5	16.2	0.6	1.1
	End moraine, BI9, impounding a lake, N 47.6035°, E 97.6403°, 2725 m asl						
	DHC-98-3	Granitic boulder	2	1.5	15.0 *	0.5	1.0

Table 1 (*continued*)

Site	Sample identification	Sample description	Maximum diameter (m)	Boulder height (m)	Exposure age (ka)	1σ uncertainty (ka)	
						Internal[a]	External[b]
	MOT98-CS-04	Granitic boulder	4	1,5	16.5	0.5	1.0
	MOT98-CS-05	Granitic boulder	2	1	16.6	0.5	1.1
Bumbat valley	*Lowest end moraine BU1, N 47.4357°, E 100.3468°, 2130 m asl*						
	HN-JB-01B	Granitic boulder	1.5	0.5	103.7	2.8	6.5
	HN-JB-01C	Granitic boulder	1	0.3	53.6	1.4	3.3
	HN-JB-01A	Granitic boulder	1	0.3	22.5	1.1	1.6
	End moraine BU2, N 47.4158°, E 100.3573°, 2172–2177 m asl						
	HN-JB-02A	Granitic boulder	2	1	22.2 *	0.9	1.5
	HN-JB-02B	Granitic boulder	1.5	0.4	39.5	1.7	2.8
	HN-JB-02C	Granitic boulder	1.5	1	31.8	1.1	2.1
	HN-JB-03A	Granitic boulder	1.5	1	36.5	1.4	2.5
	HN-JB-03B	Granitic boulder	2	1	31.8	1.8	2.5
	HN-JB-03C	Granitic boulder	0.8	0.4	49.9 *	1.8	3.3
Non-glacial deposits	*Boulders on rock/debris fall, N 46.6068°, E 93.5628°, 3205 m asl*						
at	MOT98-CS-20	Quartz vein in schist boulder	0.5	0.5	0.9	0.1	0.1
Sutai range, SW slope	MOT98-CS-21	Quartz vein in schist boulder	0.6	0.1	1.6	0.1	0.1
	Schist bedrock strath terrace, N 46.6160°, E 93.5639°, 3273 m asl						
	MOT98-CS-08	Quartz vein in schist boulder	4	0.5	11.9	0.4	0.8
	Boulders on schist strath terrace, N 46.6168°, E 93.5645°, 3290 m asl						
	DHC-98-17	Quartz vein in schist boulder	3	0.5	4.1	0.1	0.3
	DHC-98-18	Quartz vein in schist boulder	0.7	0.2	18.3	0.6	1.2
	MOT98-CS-19	Quartz vein in schist boulder	0.5	0.5	0.9	0.1	0.1
	Boulders on protalus rampart overlying strath terrace, N 46.6176°, E 93.5656°, 3310 m asl						
	SUT-IM-01A	Quartz vein in schist boulder	0.6	0.2	2.6	0.1	0.2
	SUT-IM-01B	Granitic boulder	0.6	0.2	2.9	0.1	0.2
	SUT-IM-01C	Quartz vein in schist boulder	0.5	0.2	2.8	0.1	0.2

Ages marked with * are outliers (see Methods section) and were not included in ELA calculations.
[a] Internal uncertainty includes uncertainties of measuring sample mass and statistical counting in the $^{10}Be/^{9}Be$ AMS absolute isotopic ratio.
[b] External uncertainty includes ^{10}Be production rate uncertainties.

the details of ^{10}Be age analyses, criteria for identifying age outliers, methods to calculate ELAs, and the explanation of the numerical model.

2.1. Cosmic-ray exposure dating

All samples were chemically prepared for accelerator mass spectrometry (AMS) using methods based on Kohl and Nishiizumi (1992). We ground the rock samples and extracted quartz from the 500–850 μm size fraction. The quartz was further purified by selectively etching in HF. We then added a carrier solution with a very low level of $^{10}Be/^{9}Be$ ($<2 \times 10^{-15}$) before extracting the Be by column chromatography. Chemical preparation of the samples identified as GN-AG, MOT98-CS, and DHC98 was done at the Cosmogenic Nuclide Laboratory, University of Washington, and the AMS analyses were done at the Center for Accelerator Mass Spectrometry, Lawrence Livermore National Laboratory. The samples identified as GN-JB, HN-JB, SUT-JB, SUT-IM, and OT-AG were chemically prepared at the Cosmogenic Isotope Laboratories, Hebrew University in Jerusalem. The $^{10}Be/^{9}Be$ ratio from numerous full procedural chemistry blanks ranged from 5×10^{-15} to 2×10^{-15}, which was at most 5% of the lowest measured $^{10}Be/^{9}Be$ ratio. AMS analyses were done at the ANTARES AMS Facility, Australian Nuclear Science and Technology Organization (Fink and Smith, 2007).

The ^{10}Be ages (Table 1) were calculated using CRONUS-Earth version 2.2 (Balco et al., 2008). We used the globally calibrated ^{10}Be sea-level high latitude spallation production rate (Heyman, 2014) of 3.99 ± 0.22 atoms g^{-1} yr^{-1} when referenced to the scaling of Lal and Stone (Lal, 1991; Stone, 2000). We assumed 2.65 g cm^{-3} for sample density. All calculations of ^{10}Be ages assumed zero erosion and burial in this study, and we did not account for neutron shielding by snow. An unlikely high erosion rate of 3 mm yr^{-1} would increase an apparent age of 20 ka by ~5% (Batbaatar and Gillespie, 2016; Online Supplement 2). A 4 month seasonal snowpack of 250 mm depth (e.g., Mitchell and Philip, 2005), a maximum for the modern Gobi-Altai, would increase an apparent age of 20 ka by <2% (Batbaatar and Gillespie, 2016). We provide the data for calculation of the ^{10}Be ages and photos of selected sampled boulders in Online Supplement 1.

Our work covered a broad, complex area and the number of dated samples per moraine was smaller than desired in order to characterize a population with a well-determined arithmetic mean and standard deviation. In studies such as this, identification of outliers is important, and commonly problematic. In order to identify outliers, we used a series of analyses in the following order: 1) calculate the mean and standard deviation for n ages grouped according to landform; 2) calculate the reduced chi-squared value, $R\chi^2$, for n ages to test if the scatter in the group age cannot be explained by analytical uncertainty alone; 3) for each sample i, calculate the normalized deviation, δ_i, from the mean calculated excluding the tested sample. Samples for which $\delta_i > 2$ were rejected as outliers; 4) test whether in sequence of moraines the ^{10}Be ages were consistent with the relative ages of the moraines inferred geomorphically; 5) recalculate the $R\chi^2$ excluding the outliers; 6) evaluate the identified outliers using Chauvenet's (1960) and Peirce's (Ross, 2003) criterion to confirm that the surviving samples contained no outliers. After excluding the outliers, we averaged the sample ages for a given landform and compounded standard deviation of the "reduced" group with the "internal" sample measurement uncertainties with the systematic uncertainties in the production and decay rates of ^{10}Be ("external" uncertainties). We report this 1σ total uncertainty as the duration of glacier advances or standstills for the given landform. We provide the equations used in the outlier analysis with descriptions in Online Supplements 1 and 2.

2.2. Equilibrium-line altitude (ELA)

We estimated the ELA for the dated lateral moraines using the

Maximum-Elevation of Lateral Moraine (MELM) method (Porter, 2001) where possible. If end moraines could be mapped, we used the Toe–Headwall Altitude Ratio (THAR) method (Porter, 2001) with a threshold value of 0.58, as estimated for northern Mongolia by Gillespie et al. (2008). In this approach the ELA may be found by

$$ELA = A_t + 0.58(A_h - A_t) \quad (1)$$

where A_h and A_t are the headwall and toe altitudes, respectively. The headwall altitudes of the modern glaciers on Sutai were measured from the visible bergschrund on Google Earth. We selected the headwall altitudes for paleoglaciers at one third of the altitude difference between the cirque floor and the top of the rock cliff (details are available in Online Supplement 2), which was a similar ratio for schrund-lines estimated in White Mountains, New Hampshire, USA (Goldthwait, 1970). In some cirques the headwall was defined as the point at which avalanche chutes ended in free air, where once the glacier shielded the rock below from erosion. However, in general there is no objective rule with which to estimate headwall altitude. At each valley, we assumed that the paleoglaciers shared the same headwall altitude, resulting in a THAR ELA that is only sensitive to toe altitude, defined as the minimum altitude of the crest of the terminal moraine. Therefore, the paleo headwall altitudes were higher than all the local ELAs, even on the southwestern slope of Sutai where there is a modern glacier.

The precision of the estimated ELAs depends on the accuracy of the GPS units (10 m) used to measure altitudes, the vertical uncertainty of SRTM data (30 m) used in Google Earth. However, the accuracy as judged by agreement among estimation strategies is significantly lower, around ~100 m (e.g., for the Sierra Nevada in the western USA: Gillespie, 1991). This low accuracy only affects the local ELA itself, and not the difference between ELAs for adjacent valleys.

The selection of a threshold value of THAR (ranges from 0.4 to 0.6) was the biggest source of inaccuracy in our study. For example, for large paleoglaciers such as at Otgontenger, the large difference between the toe and headwall altitudes (~1300 m) leads to a large uncertainty (~130 m) in the ELA. Small cirque glaciers (and their ELAs), on the other hand, are constrained to lie in a narrow range of altitudes, and their uncertainties can approach the measurement precision.

The Accumulation-Area Ratio (AAR) method of ELA estimation depends on an accurate reconstruction of the paleoglacier extent, which in turn requires accurate information on the headwall altitude and also the thickness of the glacier in order to delimit the ice areas. We did not use the AAR method, normally considered to be the most accurate, to estimate the ELAs, because of the complexity of the outlines of many of the studied paleoglaciers and because of the strong differences in the long profiles of the glaciated valleys we studied.

The local ELA values for a glacial sequence were normalized against the altitudes of the headwall and the minimum ELA for the sequence to compare the magnitudes of ELA lowering for the dated moraines using equation (2):

$$ELA_{norm} = \frac{A_h - ELA_{dated}}{A_h - ELA_{min}} \quad (2)$$

where ELA_{norm} is the normalized ELA, A_h is the headwall altitude, ELA_{dated} is the ELA for the dated moraine, and ELA_{min} is the ELA for the lowest end moraine in the valley, whether it was dated or not. Thus, ELA_{min} corresponds to the local LGM advance.

2.3. Surface-energy balance model

We followed the methods of Rupper and Roe (2008) to calculate potential ablation as a function of air temperature (T_a) (see detailed explanation and references for the surface-energy balance model in their original article). Our exercise was not intended to simulate actual glaciers, but rather to demonstrate the variation of ablation via melting and sublimation due to changes only in T_a, which decreases with increasing altitude via the locally measured summer adiabatic lapse rate (8 °C km^{-1}: Online Supplement 1). This lapse rate was derived from T_a measured atop the Sutai ice cap at 4000 m asl and the daily mean T_a data from the town of Tonhil 40 km to the southeast and at 2200 m asl (National Oceanic and Atmospheric Administration (NOAA), 2016). Because the T_a at Sutai was measured on an ice surface the derived lapse rate of 8 °C km^{-1} is probably greater than environmental lapse rates derived from measurements on land. We used monthly mean reanalysis climate data for the Gichginii range (Kalnay et al., 1995), scaled so that the summer (JJA average) T_a was zero at 3000 m asl, a condition equivalent to −6 °C decrease from modern T_a. This constraint on the range of T_a in the model may appear to be arbitrary, but it provides an altitude dependency (i.e., decrease) in T_a that is similar to modeled MIS 2 conditions in the Gobi (Annan and Hargreaves, 2013) and it captures the seasonal and annual variability of T_a in the Gobi. Incoming shortwave radiation was reduced due to an assumed summer ice albedo of 0.6 (e.g., Cuffey and Paterson, 2010, pp. 146) and was taken to be constant at all altitudes. We then calculated incoming longwave radiation from T_a under clear sky. The outgoing longwave radiation was calculated from the ice-surface temperature (T_s), which iteratively solved to balance all the energy fluxes, including turbulent sensible and latent heat fluxes. If T_s was positive, it was reset to zero and the net energy flux was calculated again to estimate melting. Major parameters and variables remained constant at all altitudes for simplicity: wind speed = 2 m s^{-1}, relative humidity = 50%, height at which wind speed and air temperature measured = 2 m, and scalar roughness lengths = 0.5 mm.

3. Results

The major results reported in this article are the mapping and dating of the local maximum glaciations in the arid to subhumid regions of central Mongolia.

3.1. Glaciations in the Gobi-Altai ranges

Gichginii range … The Gichginii range (Figs. 2 and 4a) lies in the central part of the Gobi-Altai, and of the five sites we studied it receives the least precipitation (~55 mm yr^{-1}; long-term data (Schneider et al., 2016) for an area 0.5° × 0.5° centered on the site). Here, a ~1.5 km^2 plateau shows cryoplanation surfaces at ~3580, ~3550, and ~3520 m asl, and it may have provided the base for a paleo-ice cap (Online Supplement 1: Fig. 2). Similar to modern ice caps at Sutai and their outlet glaciers, this putative paleo-ice cap on the Gichginii plateau appears to have spilled north into the upper Mönh Mösnii valley. The Gichginii plateau consists of dark schist, but the northern wall of the Mönh Mösnii cirque consists of light tan-weathering gray limestone. The southern side of the cirque is a steep (~30°) headwall of schist bedrock which grades down via modern talus beneath bottomless avalanche chutes into a ~15° northeast-sloping cirque floor. The avalanche chutes terminate about 70 m below the plateau, below which where ice once shielded the lower headwall from erosion and deposition; in nearby unglaciated valleys the avalanche chutes reach the valley floors. At least five diamicton ridges were deposited on the cirque

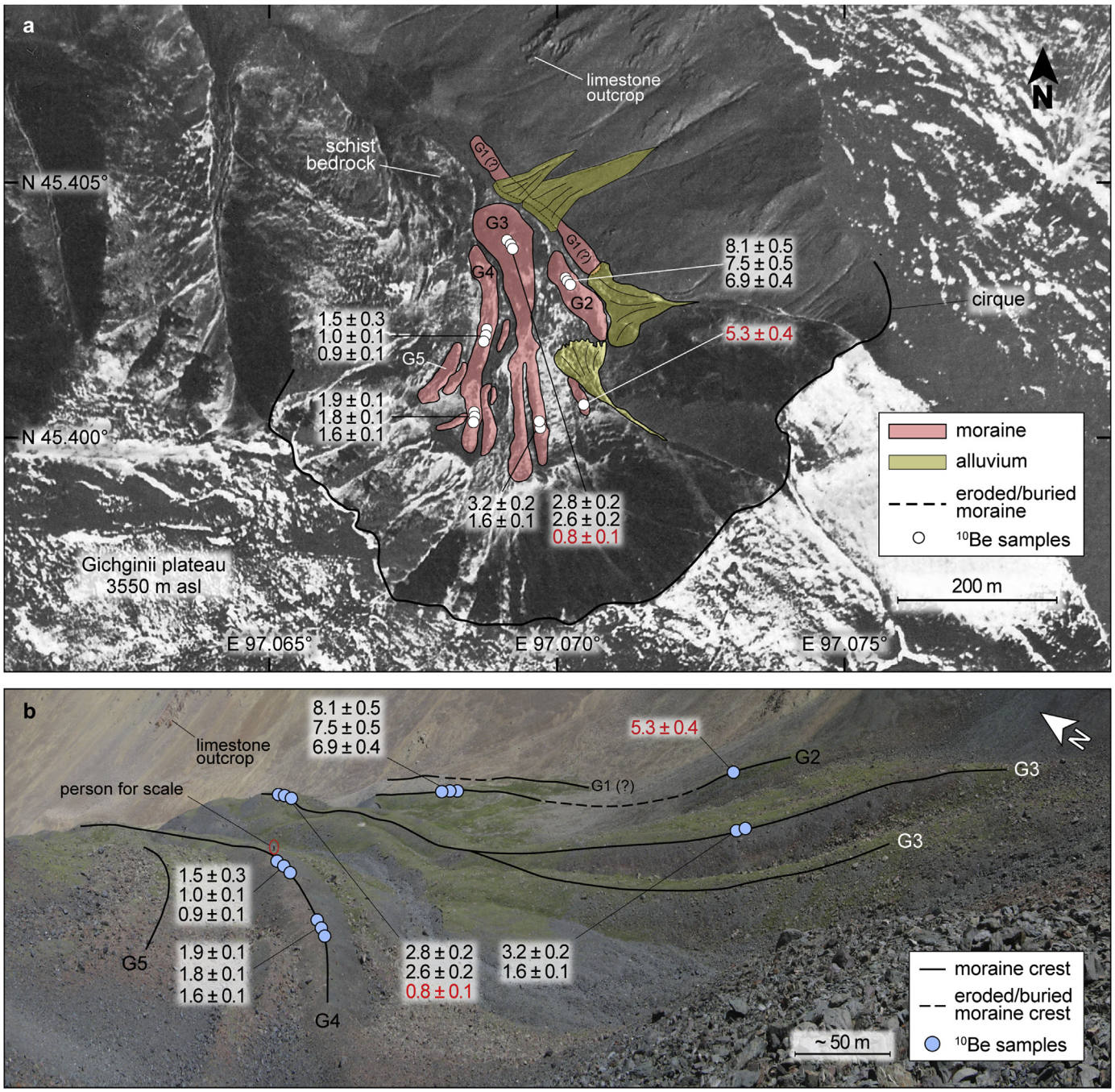

Fig. 4. Moraines in the Mönh Mösnii valley, Gichginii range, and locations of ^{10}Be ages. a. Aerial photo (National Archives of Mongolia, acquisition winter of 1957) showing sample locations and moraine locations. b. Field photo showing the moraines and ^{10}Be exposure ages. Ice flow was from south to north. ^{10}Be exposure ages are in ka ± 1σ. Rejected ages are shown in red.

floor as much as 250 m below and ~0.6 km from the plateau. The clearly separated linear–arcuate ridges rise ~30 m above the valley floor and within the deposit have a relief of 3–4 m. At the lower edge of the cirque the ridges sit atop schist bedrock. The long profile of Mönh Mösnii valley is concave-convex-concave, typical of glaciated valleys, and the ridges spill over the bedrock lip of the cirque and down to the concave portion of the valley, a vertical distance of ~50 m below.

The lowest ridge in the cirque, G1, was eroded and remnants were buried by limestone boulders and scree from the northeast, and capped by ~10 cm of loess. Its light color is in sharp contrast with the dark schist of the four inner ridges, with which it is slightly discordant (Fig. 4b). Although G1 may be an old moraine, it is also possibly a kame terrace impounded against a cirque paleoglacier. No schist boulders (with their included quartz lenses) were found on its surface; thus, there were no opportunities for ^{10}Be dating.

In contrast, moraine ridges G2–G5 (Fig. 4) consist of sub-angular schist diamict sourced in the south from the Gichginii plateau. G2–G4 are stable and vegetated, and the surface boulders host lichens. Their lack of flow features on or between the ridges argues against an origin as rock glaciers (e.g., D. Trombotto Liaudat, pers. comm., 2017) (see the surface features in Online Supplement

1: Figs. 3–6).

We sampled every boulder that we could find in the Mönh Mösnii cirque large enough and containing enough quartz lenses to permit the ^{10}Be dating. Four ^{10}Be ages from moraine G2, the oldest dated moraine, were measured and, after excluding one outlier (i.e., n = 3), indicate glacial deposition during ~8–7 ka. Approximately 40 m above the G2 moraine, four boulders on the G3 moraine (Fig. 4) were dated to ~3–2 ka, after excluding one outlier. The youngest moraine we dated, G4, lies at about the same altitude as G3, and six boulders from there gave an age range of ~2–1 ka (Online Supplement 1: Fig. 7). In the field, G5 appeared to us to be similar to Little Ice Age moraines elsewhere (LIA: after ~0.7 ka, Matthews and Briffa, 2005). The ELAs associated with G1–G5 were 3320, 3330, 3360, 3365, and 3370 m asl, respectively. In contrast, the ELAs for the LIA paleoglaciers along the Mongolian–Siberian border (Mönh Saridag peak) 750 km to the NNE were ~3190 m asl (Batbaatar and Gillespie, 2016) about 180 m lower than G5. The MIS 2 ELA in the northern Mongolia (Darhad basin) was ~2100 m asl (Gillespie et al., 2008), about 1220 m lower than for G1. Thus, the total range of ELAs in northern Mongolia was much greater than in the arid Gichginii range.

The undated G1 feature, which marks the extent of the local LGM in the Gichginii range, lies only ~10 m lower than the crest of the G2 moraine, and therefore the ELAs are nearly the same. Whatever the age of G1, the G1 and G2 paleoglaciers were similar in size and extent. The valley below the cirque is characterized by a fluvial, ~10 m deep bedrock inner gorge downslope from the talus. The bedrock gorge could have been cut by subglacial streams if the paleoglaciers ever advanced beyond G1. Otherwise, we found no evidence of a glacial advance in the Gichginii range during the global LGM, a cold period of permafrost presence in the Gobi-Altai (Owen et al., 1998). If the Mönh Mösnii valley below the cirque was ever glaciated, it was long enough ago that the moraines have all been removed by erosion.

Sutai range … The Sutai range in the western end of the Gobi-Altai hosts three modern ice caps (referred to as # 1, 2, and 3 in Fig. 5a). The two largest (#2 and 3) occupy a high plateau southeast of our studied valleys and are narrowly separated today but probably merged during major glaciations. Ice cap #2 feeds at least five well-developed glaciers that descend both the northeastern and southwestern slopes of Sutai. Three boulders from a series of lateral moraines on the northeastern slope, NE2–4 in Fig. 5b, were dated to ~27–22 ka, after rejecting an outlier of 6.7 ± 0.4 ka. We also rejected a single ^{10}Be age of 7.3 ± 0.5 ka from the lowest end moraine a few hundred meters down valley as it appeared too young for the landform relative to its neighbors.

The pass between ice caps #1 and #2 is now occupied by a modern outlet glacier flowing west from ice cap #2. Most of the glacier now flows south and descends down a canyon on the SW side of the ridge, but in the past it also descended to the NE outlet valley (Fig. 5a and b). About 20 m higher than the glacierized pass is a lateral moraine on the ridge leading to ice cap #1. Deposition there likely resulted from the bedrock ridge diverting both to the northeast and southwest the paleoglacier flowing into the pass. The altitude of this marginal moraine reflects the local depth of the outlet glacier, but not its maximum extent. Given its location, it may even be time-transgressive. We collected three samples from the crest of this moraine: two above the pass itself (~45 ka and ~13 ka) and a third 83 m to the south (~25 ka). The two younger ages could be consistent with the MIS 2 ages from below the pass to the NE. Exactly how this moraine remnant fits into the chronostratigraphic sequence is unclear, however, and with only three ages widely separated in time, an age for the moraine cannot be determined with any confidence.

Near the margins of ice cap #3 on the Sutai plateau, we sampled two erratics (Fig. 5c). The erratics were dated to ~42 and ~21 ka, echoing the disparity of the three ages from the pass. These did not allow us to determine an age relevant to the paleo-ice cap. Viewed collectively, the five samples from the Sutai plateau and the pass began their exposure histories at different times during MIS 2 and 3. More work will be required to unravel their significance.

On the southwestern piedmont of Sutai (Fig. 5a and c), we dated eight more samples, including six from a right-lateral moraine complex. Four of five boulders from the crest of SW2 right-lateral moraine yielded ages of ~19–13 ka, with the other being rejected as an outlier. Another boulder from what in the field appeared to be a remnant of a recessional moraine was dated to ~36 ka, which clearly was too old for its context. We also sampled an isolated glacially eroded bedrock knob at 3105 m asl, ~75 m lower altitude than the preserved moraines and ~0.8 km downslope. The knob has not been heavily weathered or eroded. It was dated to ~22 ka, not inconsistent with the younger SW2 right-lateral moraine. A nearby glacial erratic boulder at the same altitude was dated to ~72 ka, however. It is possible that the erratic simply contained inherited ^{10}Be and is anomalously old; it is also possible that it once sat atop the now-eroded moraine that buried the bedrock knob, but was too large to move or erode completely. In this interpretation, the ^{10}Be age of the erratic might be a minimum for the moraine, and the age of the knob may simply reflect exposure since erosion of the moraine.

Like the lowest right-lateral moraine, all the left-lateral moraines are missing from the piedmont. We sampled two boulders from what appears to be soliflucting debris where we expected the moraine once was. The debris could have originated as rockfall, possibly triggered by range-front faulting. The two boulders were dated to ~1.6 and 0.9 ka (Fig. 6a). The evidence of mass wasting from the range front suggests that seismicity in the region in addition to active permafrost processes may have modified the initial exposure position of the boulders there.

Strath terraces formed just above the southwestern piedmont of Sutai after the glaciers receded from their last maximum positions (Fig. 6a and b). Four boulders on the strath terraces and three more from a protalus rampart burying the terraces yielded wide-ranging ages of ~18–1 ka, and a tight cluster of 3–2.5 ka, respectively.

Ih Bogd range … Near the easternmost end of the Gobi-Altai, the Ih Bogd range provides evidence of glaciation with well-developed cirques and moraines (Fig. 7a). The best-preserved evidence on the southern side of Ih Bogd is in Artsan valley, where moraines from at least six advances, labeled as IB1–IB7 in Fig. 7b, sit ~150–500 m from and 30–130 m below the headwall. A single boulder from the youngest moraine was dated to ~14 ka. Five boulders ~25–35 m down valley, from a series of lateral and end moraines, IB5–6, gave ages that ranged from ~17 to 13 ka. We rejected a^{10}Be age of 7.3 ± 0.6 ka from the IB5 moraine as an outlier. The altitude of the most distal moraine (IB1, not sampled) was only ~50 m below the IB5 moraine.

3.2. Glaciations in the Hangai ranges

In the dry subhumid zone to the north of the three sites in the Gobi-Altai, the Hangai ranges were heavily glaciated before and during the global LGM (Rother et al., 2014), with separate peaks supporting their own ice caps. Otgontenger is the only peak high enough today to preserve a small ice cap. In the Bogd river valley, on the western side of Otgontenger (Fig. 8a), Rother et al. (2014) concluded on the basis of ^{10}Be dating that the outlet glaciers advanced to the local LGM at ~38 ka during MIS 3, but that the MIS 2 glaciers were comparable to or slightly smaller than the MIS 3 glaciers. Three glacial boulders we sampled from the lowest terminal moraine in the Bogd valley dated to ~25–20 ka, consistent

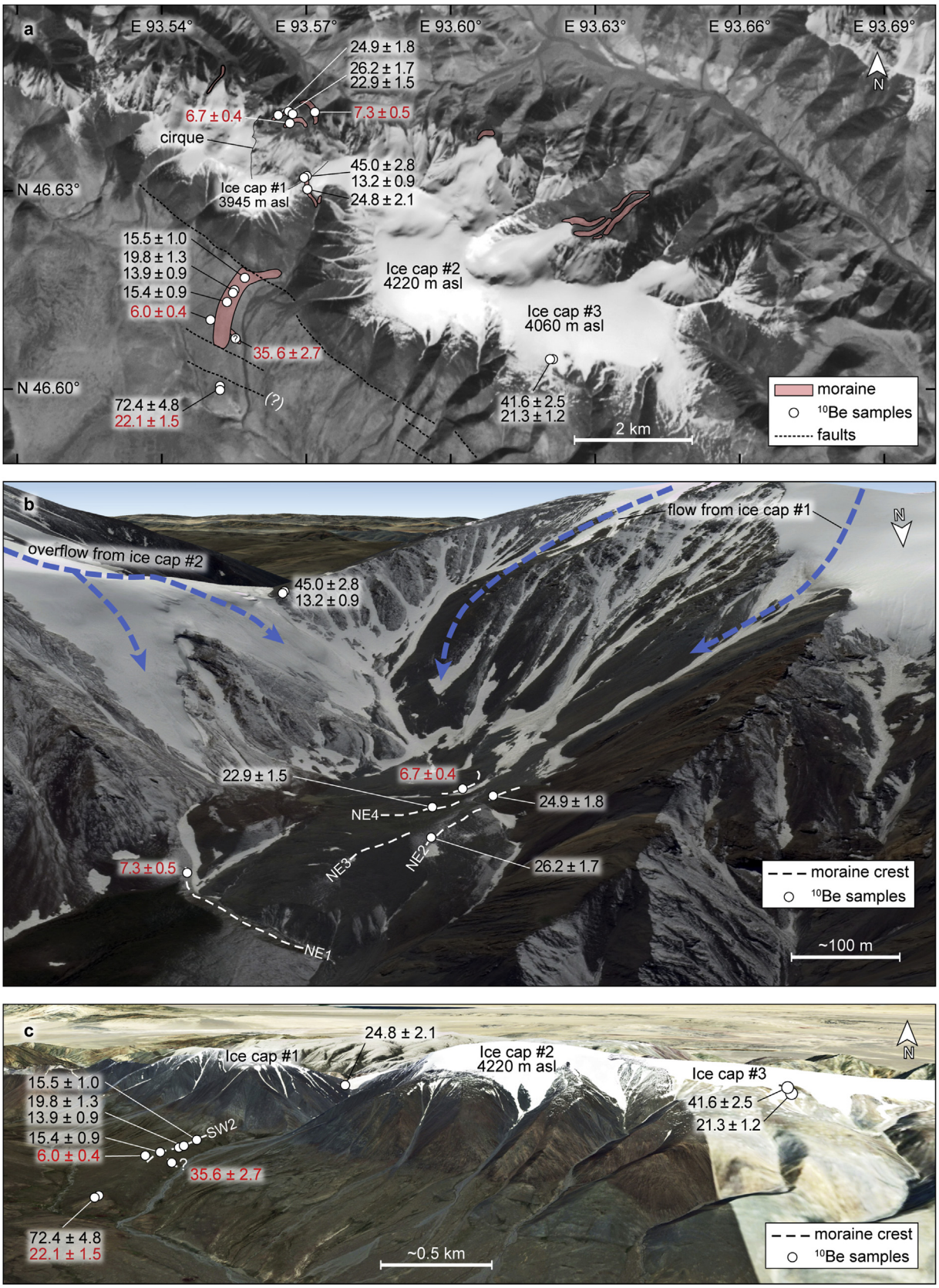

Fig. 5. Sample locations in Sutai range. a. ASTER image (September 21, 2003; band 3N) showing the southwestern and northeastern slopes of the Sutai range and the ^{10}Be ages for glacial deposits. b. Google Earth perspective view of the moraines in the northeastern slope. c. Google Earth perspective view of the moraines in the southwestern slope. The glaciers in the studied valleys are both fed by ice cap #2. ^{10}Be exposure ages are in ka ± 1σ. Rejected ages are shown in red. Google Earth overlay is the DigitalGlobe and Landsat images acquired in June 2013.

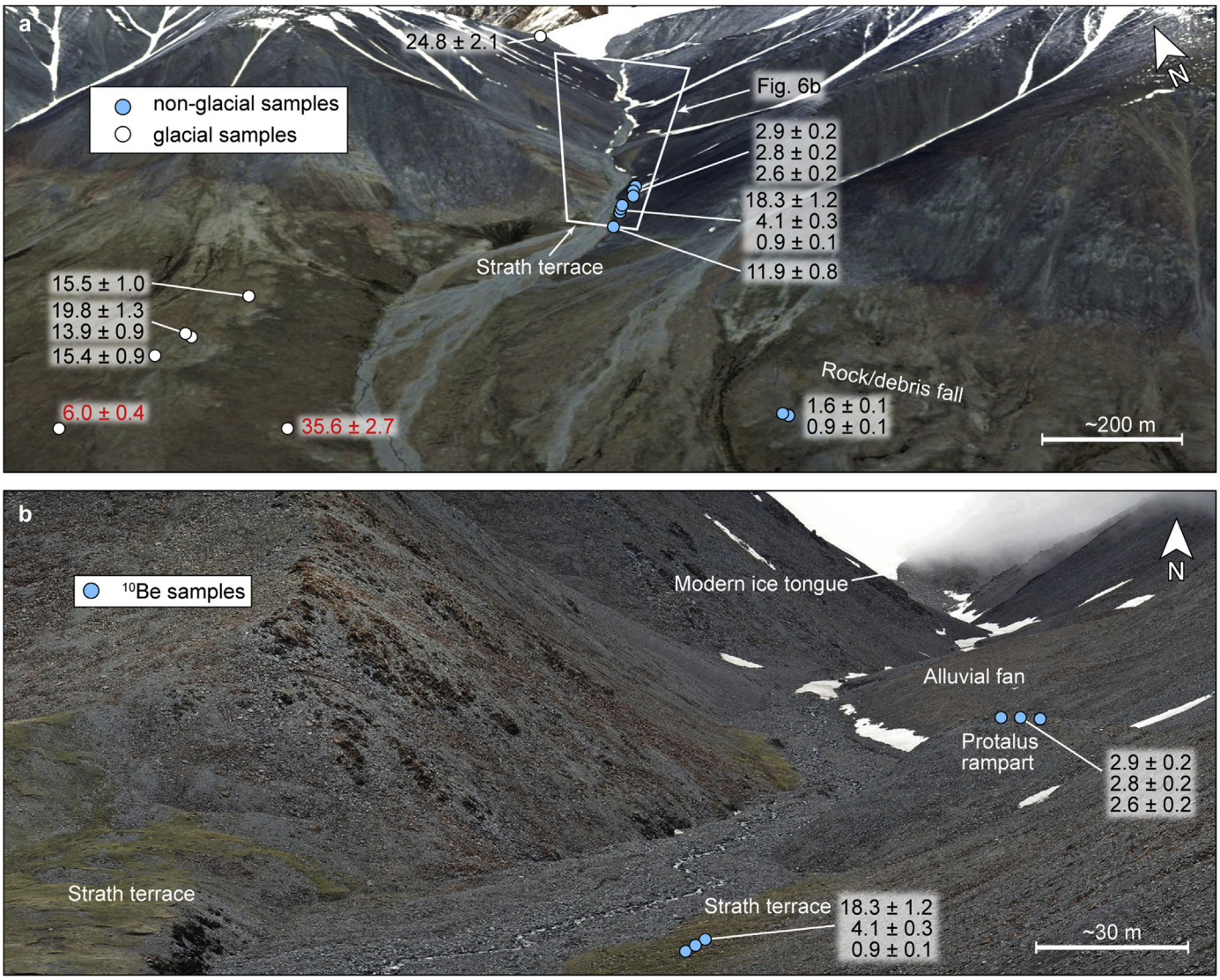

Fig. 6. Non-glacial samples at Sutai. a. Google Earth perspective view of the southwestern slope and the locations of the glacial (white circles) and non-glacial (blue circles) samples. b. Field photo showing a closer view of the strath terraces on both sides of the stream and protalus rampart and alluvial fan covering the terraces. Numbers refer to ^{10}Be ages, in ka ± 1σ. Rejected age is shown in red. Google Earth overlay is the DigitalGlobe image acquired in June 2013.

with the findings of Rother et al. (2014). To extend the glacial history at Otgontenger, we dated glacial boulders in the Bitüüt valley (Fig. 8a and b) on the eastern side of Otgontenger. Bitüüt valley is a separate drainage from the Bogd valley, although the outlet glaciers in these valleys probably were sourced from the same ice field. We sampled from three moraines that comprise part of a retreat sequence of at least ten moraines (BI1 to BI9) in the Bitüüt valley. Two boulders from one of the oldest Bitüüt end moraines (BI2) were deposited at ~33–28 ka. A third boulder was dated to ~83 ka and was rejected as an outlier. About ~1.4 km upvalley and an additional ~120 m rise in altitude from the lowest two moraines, three ^{10}Be ages for boulders on the two younger moraines, BI8 and BI9, ranged in age from ~17 to 16 ka (Fig. 8b). The boulder age of 15.0 ± 1.0 ka from BI9 was rejected as an outlier.

To complement the chronology of glacial advances in the Hangai ranges, we traveled approximately 200 km east of Otgontenger, and sampled two moraines in another glaciated valley, the Bumbat. Three boulders on the older moraine, BU1 in Fig. 9a, gave wide-ranging ages of ~104, 54, and 23 ka. Four of six ^{10}Be ages from a younger inner moraine 2.5 km upvalley (BU2 in Fig. 9) suggest a deposition age of ~39–30 ka. The other two ^{10}Be ages of 49.9 ± 3.3 ka and ~22.2 ± 1.5 ka, were rejected as outliers (see details of outliers in Online Supplements 1 and 2).

3.3. Mechanisms of ablation in the Gobi-Altai and Hangai ranges

The reconstruction of paleoclimate from glacial records relies on the empirical relationship between summer T_a and annual precipitation at the ELAs (Ohmura et al., 1992). This approach has recently been extended to arid and semiarid regions in Central Asia (Sakai et al., 2015) (Fig. 10) using GAMDAM glacier inventory compiled using satellite images and high-resolution climate data (Nuimura et al., 2015). On this annual precipitation vs. summer T_a diagram, we have also plotted the modern climate data (Kalnay et al., 1995; Schneider et al., 2016) at the modern ELA for existing glaciers and at cirque headwalls for currently unglaciated valleys covering the five regions we have studied (black filled symbols in Fig. 10). Unsurprisingly, the modern glacier at Sutai and the Otgontenger ice cap plot within the limits for glaciation today, but the other three sites are too warm and dry, and plot outside

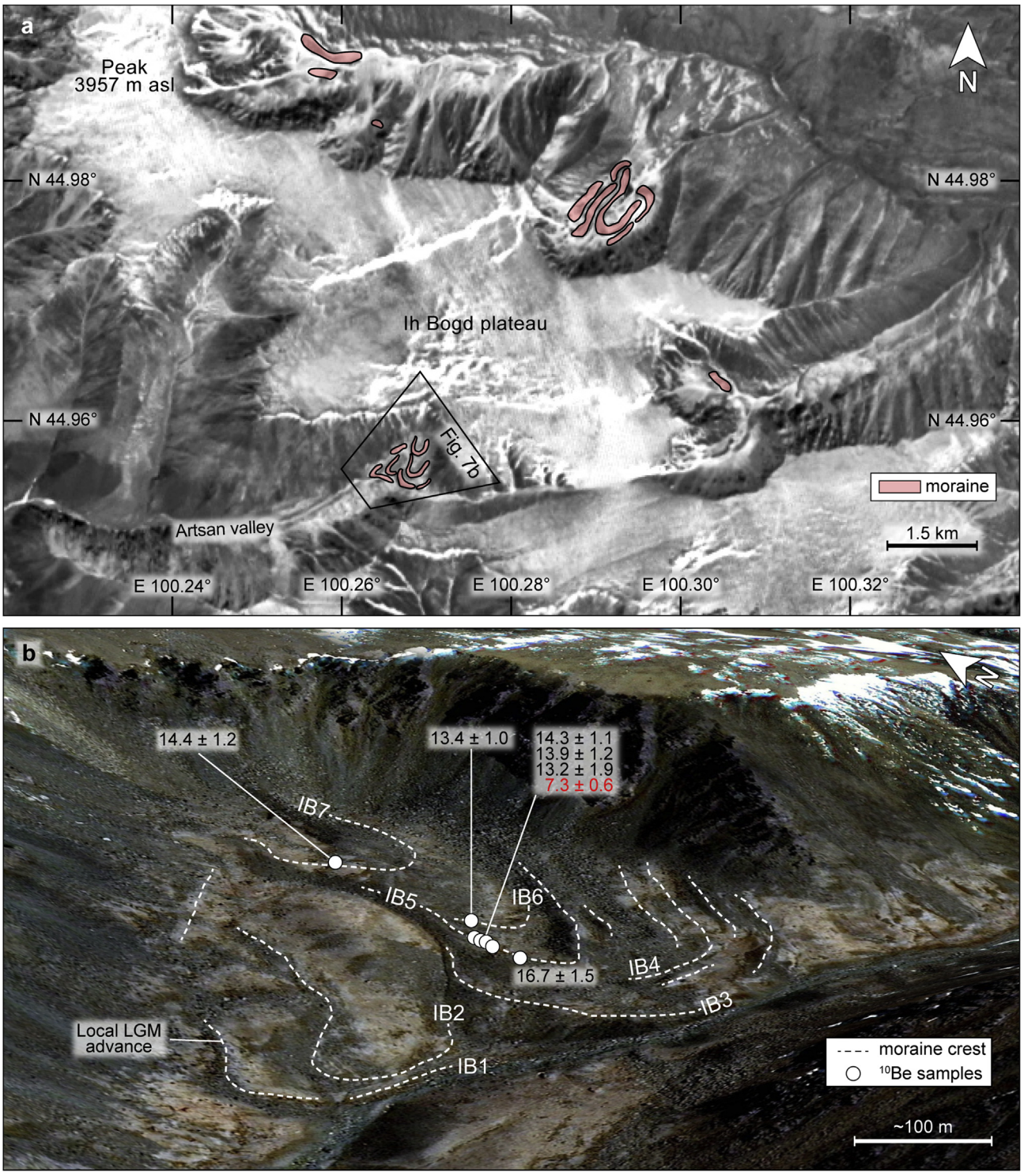

Fig. 7. Ih Bogd range and the ^{10}Be sample locations. a. ASTER image (acquisition April 14, 2001; band 3N) showing the cirques with glacial deposits. There is no modern ice on the plateau, and snow is covering the white areas on the image. b. Google Earth perspective view (background: DigitalGlobe image acquired in June 2007) showing the dated moraines in the Artsan valley. ^{10}Be exposure ages are in ka ± 1σ. Rejected age is shown in red.

the limits. We then projected the estimated MIS 2 climate (Owen et al., 1998; Braconnot et al., 2007; Bintanja and van de Wal, 2008; Annan and Hargreaves, 2013) to the MIS 2 ELA for the studied paleoglaciers (open symbols, Fig. 10) onto the diagram. All the estimated MIS 2 data points plotted well within the allowed glaciation zone defined by the modern glacier data, apart from Gichginii site, which appears to be marginal. This suggests that Gichginii may have been too dry to support glaciers during MIS 2, in agreement with the absence of MIS 2 deposits. Had the MIS 2 precipitation at Gichginii marginally higher than the modern value, the Gichginii range would have been glaciated then. For the early Holocene, the modeled summer T_a was 3 °C warmer than

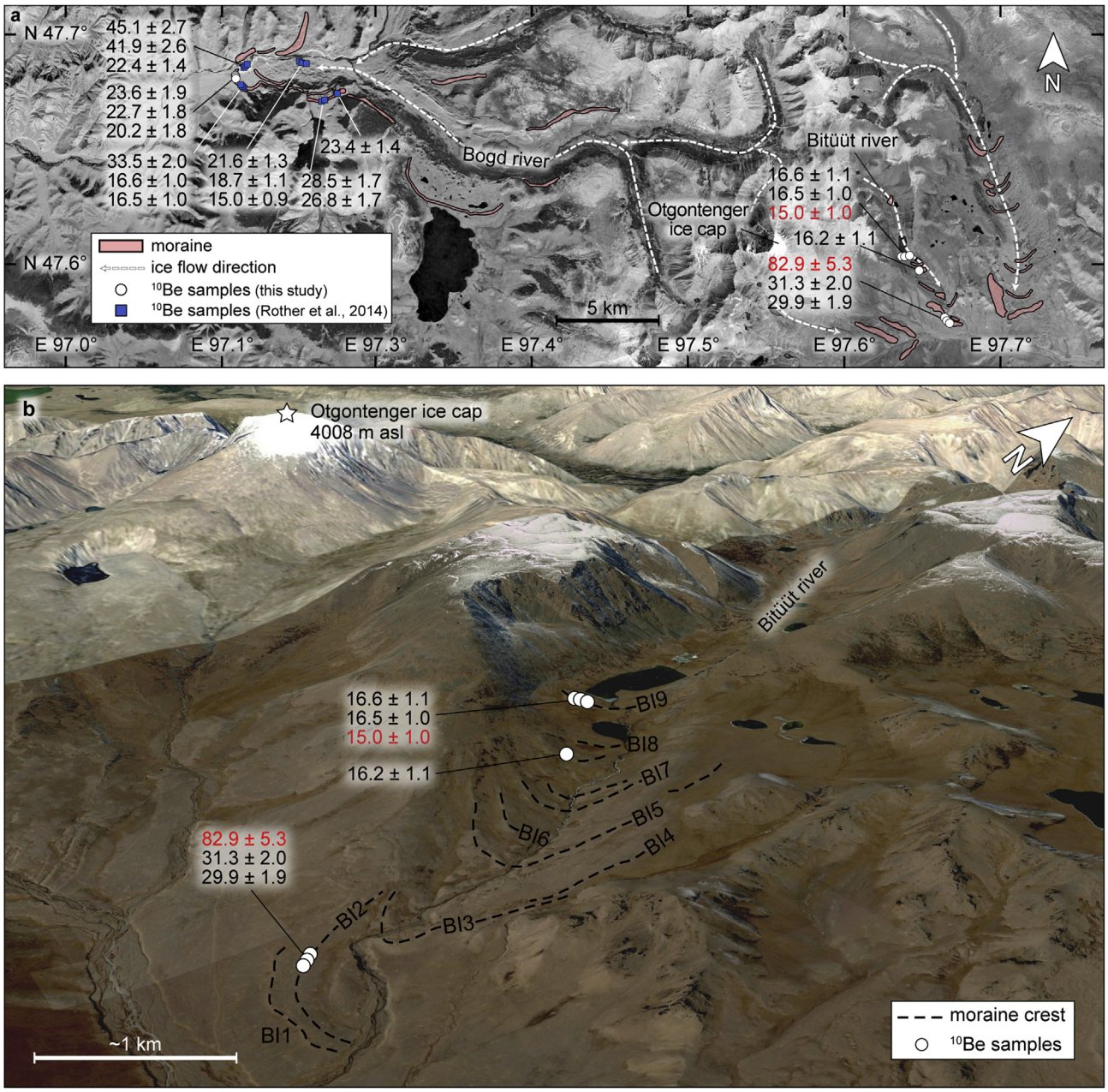

Fig. 8. Otgontenger site and sample locations. a. map showing prominent moraines and sample locations from this study and Rother et al. (2014). The glaciers from MIS 2 were slightly smaller than from MIS 3, but comparable in size. b. Google Earth perspective view (DigitalGlobe image acquired in October 2011) shows the sets of moraines in the Bitüüt valley east of Otgontenger. ^{10}Be exposure ages are in ka ± 1σ. Rejected ages are shown in red.

today (Jin et al., 2012), which would have been too high to have enabled glaciation per Fig. 10. However, the existence of Gichginii cirque glaciers requires that snow did survive the summers in the early Holocene; thus, it may be impractical to reconstruct summer T_a for small cirque glaciers in cold, arid conditions using this empirical curve.

We calculated the rates of melting and sublimation at altitudes of 2000–3500 m asl to examine the ablation mechanisms of a glacier in cold and arid conditions. Our surface-energy balance model suggests that at lower altitudes (i.e., red zones in Fig. 10 or 11a–d) high T_a provides excess energy available for melting (Fig. 11b). At higher altitudes and cold climates (i.e., blue zones in Fig. 10 or 11a–d) sublimation dominates ablation where melting cannot occur (Fig. 11c). For example, at 3500 m asl, approximately the lowest limit of the Gichginii plateau, direct insolation exceeds net longwave radiation during the summer (Fig. 11e) but T_a remains low enough that ice cannot melt (Fig. 11f) and the excessive energy is spent to sublimate it (Fig. 11g).

The normalized ELAs in Fig. 12a for the Gobi-Altai and Hangai ranges show the timing and the magnitude of the glacial advances compared to the normalized ELA depressions of the local LGMs (100%). At Gichginii, the ELA_{norm} depression indicated by the early Holocene G2 moraine (8–7 ka) (Fig. 4) was ~90% of the value for the lower undated G1 ridge (Fig. 12a), assuming the latter was glacially deposited. On the other hand, if G1 was non-glacial then the local LGM occurred during early Holocene, as registered by G2.

Sutai hosts modern glaciers on both SW and NE slopes. The ELA depression of the dated MIS 2 glaciers on the NE slope was ~80% of

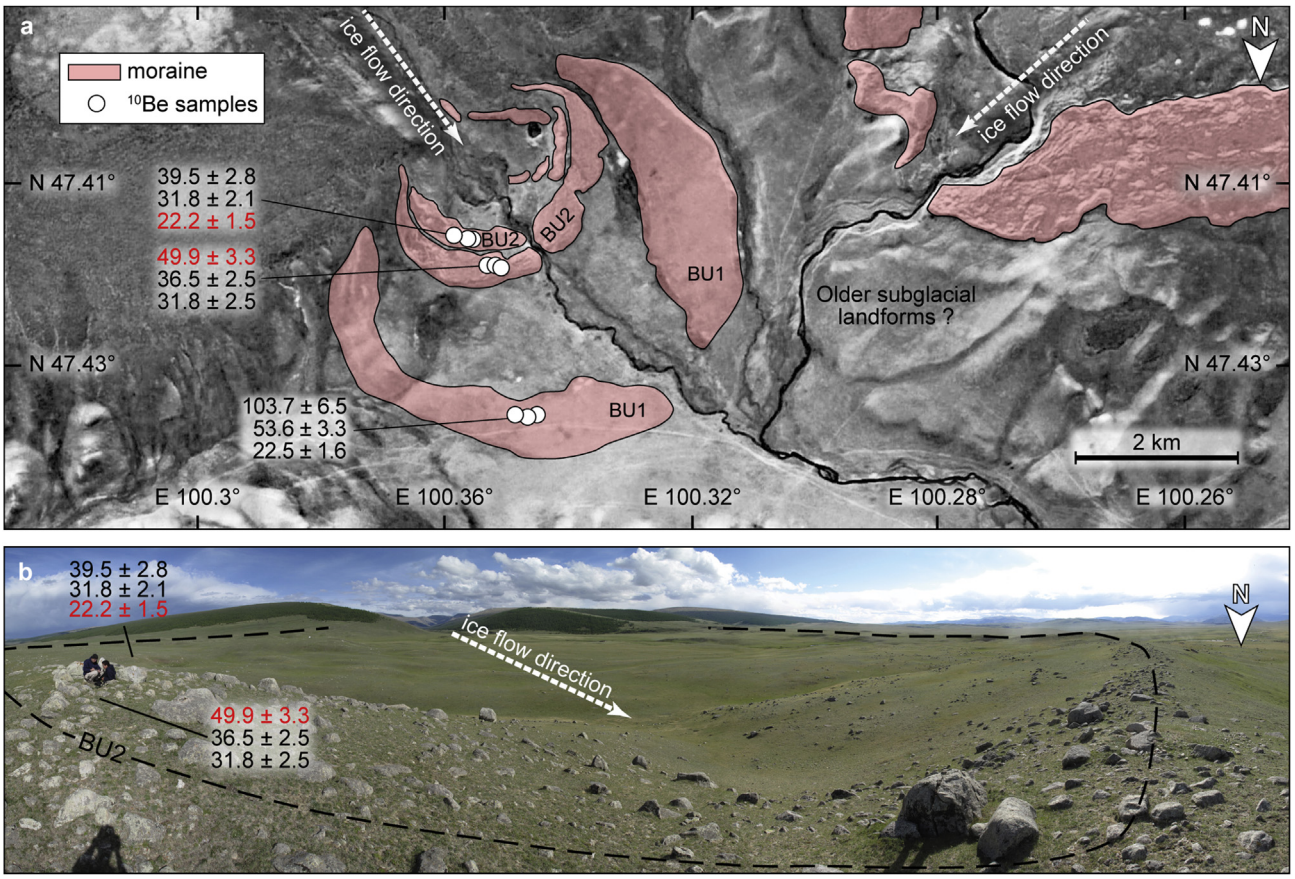

Fig. 9. The moraines at the Bumbat site, Hangai ranges. a. Map showing the end moraines and locations of the ^{10}Be samples (background is Landsat image from Google Earth). b. Panoramic photo looking southeast showing the surface of the younger end moraine crest (dashed lines). ^{10}Be exposure ages in ka ± 1σ. Rejected ages are shown in red.

undated local LGM glacier, and the small modern glacier from the ice cap #1 at Sutai had an ELA_{norm} of ~40% (Fig. 12a). The glacially eroded bedrock knob (MOT98-CS-22: 22.1 ka) on the SW piedmont of Sutai suggests that the local LGM glacier on the piedmont occurred during MIS 2 (or earlier), but the set of four ^{10}Be ages ranging from ~20 to 14 ka on the right lateral moraine only 130–160 m higher in altitude suggests that extensive paleoglaciers persisted or re-advanced on the piedmont late in MIS 2. The ELA depression of the modern glacier on the SW slope of Sutai was at 28% of the depression during the local LGM.

There are undated local LGM moraines in Ih Bogd range and the ~17–12 ka moraines there were projected in Fig. 12a to have ELA depression of ~70% the value for the local LGM glacier. The paleoglaciers in all studied valleys in the Hangai ranges, Bogd, Bitüüt and Bumbat, achieved their local LGM extent during MIS 3, not MIS 2 (Fig. 12a). The modern $ELA_{norm} = 0$ at Otgontenger, because the top of the modern ice cap of Otgontenger lies more than 500 m above the headwall.

4. Discussion

4.1. Glacial asynchrony due to differences in climate and the variations of local conditions

The timing of the local LGM in the Gobi-Altai and Hangai ranges (Fig. 12a) reveals three modes of glacial behavior and/or timing: 1) in dry subhumid regions—Otgontenger and Bumbat—the MIS 3 glaciers were larger than during MIS 2; 2) in semiarid regions—Sutai and Ih Bogd—MIS 2 glaciers were the largest; and 3) in arid regions—Gichginii— the early Holocene glaciers were as large as the local LGM. Regional changes for the last 60 ka in climate parameters that control the glacier mass balance, such as snowfall (Fig. 12b), air temperature T_a (Fig. 12c), and seasonality (Fig. 12d) explain the glacial asynchrony in all these regions. In particular, greatly reduced regional precipitation can explain the unusual restriction of MIS 2 glaciers to their cirques in some ranges. In normally cold and arid desert ranges, increased precipitation modified by unusual local conditions provided additional accumulation of snow and reduced ablation, which amplified the glacial asynchrony there.

For example, at Sutai any MIS 3 glaciers appear to have been over-run by glaciers during MIS 2. This is consistent with the "synchronous" hypothesis, in which the extent of mountain glaciers and high-latitude ice sheets co-varied closely through time. In contrast, the MIS 3 glaciers in the Hangai ranges extended further down the valley than the glacial advances during MIS 2, the global LGM, observations consistent with earlier studies (Rother et al., 2014). The pattern is consistent with glacial records in the humid Sayan ranges in southern Siberia, where the ELA during MIS 3 was ~75 m lower than during MIS 2 (Gillespie et al., 2008; Batbaatar and Gillespie, 2016). Larger MIS 3 glaciers are not predicted by the "synchronous" hypothesis, since the global ice volume was maximized during the MIS 2 global LGM. Regional precipitation and effective moisture in Central Asia (Fig. 12b) were greater during MIS 3 than MIS 2 (Herzschuh, 2006), and this likely contributed to the larger MIS 3 glaciers in the Hangai ranges. After ~28 ka the climate became drier and colder (Fig. 12b and c). Seasonality, which had been quasi-stable throughout MIS 3, started to change at the

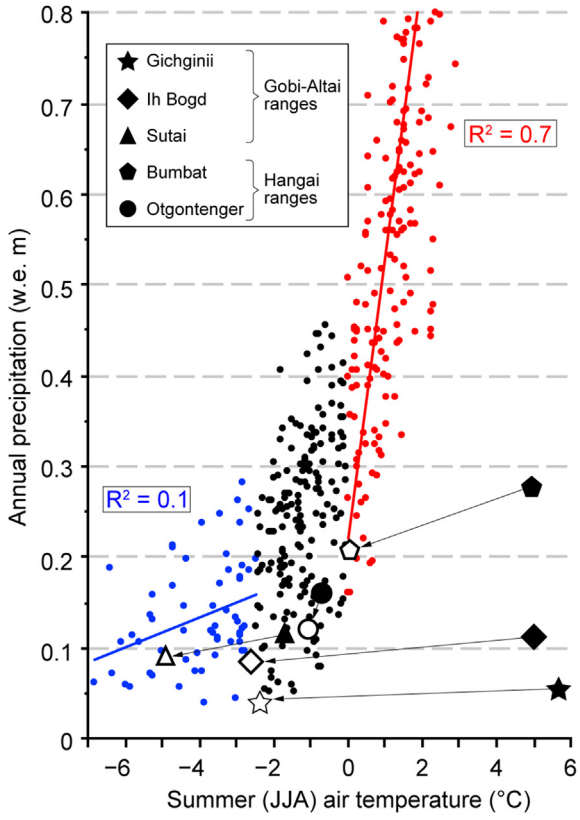

Fig. 10. The relationship between annual precipitation and summer air temperature at the ELA for modern glaciers in Asia. The data are taken from the GAMDAM glacier inventory (Sakai et al., 2015). Blue dots indicate summer temperatures below −2.5 °C; red dots indicate summer temperatures above zero. At the lowest temperatures ablation is dominated by sublimation (~50–100 mm yr^{-1}) ("precipitation-sensitive regime") and is insensitive to air temperature; in warmer climates ablation depends more on air temperature (300 mm K^{-1}) ("temperature-sensitive regime"). Solid black symbols represent today's climate at the modern ELA for Sutai (3870 m asl) and Otgontenger (3800 m asl), and headwall altitudes for currently unglaciated valleys (Gichginii 3440; Ih Bogd: 3500; Bumbat: 3080 m asl) were used in place of the ELA. Open symbols represent estimated MIS 2 climate with air temperature = modern −8 °C (Owen et al., 1998; Bintanja and van de Wal, 2008; Annan and Hargreaves, 2013) and precipitation at 75% of modern (Braconnot et al., 2007) at the MIS 2 ELA (Sutai: 3280; Otgontenger: 2850; Gichginii: 3440; Ih Bogd: 3450; Bumbat: 2690 m asl). Precipitation data are from the GPCC 0.5° v7, long-term (1981–2010) monthly mean (Schneider et al., 2016). Temperature data are from the NCEP/NCAR 2.5° long-term (1981–2010) monthly mean (Kalnay et al., 1995) scaled to the altitude with lapse rate of 8 °C km^{-1}. The region outside the envelope defined by the red/blue data points fall into two categories: above and left, the climate is wetter and/or cooler than at the ELA and would correspond to an altitude within the accumulation zone; below and right of the data points the climate is too dry and/or warm to support glaciers (i.e., within the ablation zone).

beginning of MIS 2: spring and summer insolation decreased (Fig. 12d), contributing to delayed melting in the spring and reduced ablation in the summer.

The clearest example of asynchronous glacial advances was observed in the Gichginii range, our most arid site in the Gobi-Altai. The lowest ridge, G1 in Fig. 4, may be a moraine remnant buried by scree and thus may mark the local LGM there, but the ^{10}Be ages from the next oldest moraine, G2 in Fig. 4, and only ~10 m higher, suggest that a glacial advance of similar ELA occurred during ~8–7 ka. Given the amount of rock excavated in making the Mönh Mösnii cirque compared to the volume of till contained in it today, it is evident that the cirque must have been occupied by Pleistocene glaciers that moved the debris down valley. Thus, the local LGM in the Gichginii range may have occurred during MIS 3 or 2, but even if it is younger, deposits from possible older advances must have been eroded or buried by the Holocene moraines G2–G5 there. This is not surprising because in cycles of glacial advances and retreats, the younger advances commonly overlap and obliterate older ones if the younger one is larger (Gibbons et al., 1984). Obliterative overlap is also a reason why glacial records from MIS 2 are much more abundant and pronounced than older ones from MIS 3 in Central Asia (e.g., Heyman et al., 2011b), and indeed throughout the world.

The early Holocene in Mongolia was a pluvial period with an almost three-fold increase in regional precipitation (Fig. 12b; Herzschuh, 2006; Miehe et al., 2007), and ~10 °C higher annual T_a than during the global LGM (Fig. 12c; Bintanja and van de Wal, 2008; Online Supplement 1). During the early Holocene, insolation increased in summer and decreased in other seasons relative to the global LGM conditions (Fig. 12d). This may have increased the snow accumulation, especially on the Gichginii paleoglaciers, by two mechanisms: 1) A weakened Siberian high-pressure system during early Holocene (Mayewski et al., 2004) allowed passage of westerly moisture late in spring and early in autumn; 2) Colder springs and autumns preserved more snow. Today, spring and autumn accounts for ~25% of annual precipitation (~55 mm: Fig. 2) near the Gichginii range and the annual T_a in these transitional seasons is approximately −9 °C at the altitude of the dated moraines (3340 m asl). Glacial advances of the early Holocene have been documented in similar westerly-dominated regions as well. For example, glaciers in eastern Sayan mountains of southern Siberia advanced at ~10 ka (Batbaatar and Gillespie, 2016). Ice-core records from the Belukha ice cap ~900 km to their southwest reveal that the existing glaciers in the Altai mountains formed ~11–7.5 ka (Aizen et al., 2016). In the semiarid southern Kyrgyz Tien Shan, glaciers of the Aksai basin may have advanced at ~8–5 ka (Koppes et al., 2008). These examples demonstrate that precipitation-driven glacial advances were not unique to the Gichginii paleoglacier during the early Holocene. However, in the Artsan valley of Ih Bogd, no Holocene moraines were found and the youngest glacial advance was ~16–12 ka, following the global LGM. The pattern in the Gobi-Altai is distinctly different from that across the Hangai range and is decidedly different than would be predicted by the "synchronous" hypothesis, in which the largest glaciations occurred at roughly the same time globally. The summary of our interpretation of the moraine ages is given in Table 2.

In addition to regional climate conditions, glacial response is modulated by local factors. This is especially true for small cirque glaciers. The Mönh Mösnii cirque in the Gichginii range faces north, and its glaciers were more shadowed than those in the south-facing valleys of Ih Bogd and Sutai. Indeed, the modern north-facing Sutai glaciers are much larger than on the south slopes. Furthermore, accumulation in catchments located downwind from the large high-altitude plateaus common in the Gobi-Altai is augmented by snow blown from them into the cirques by the strong prevailing westerly winds. The Mönh Mösnii valley in the Gichginii range is downwind (east) of a summit plateau (Online Supplement 1: Fig. 2), three times the area of the cirque (0.5 km^2), increasing the effective accumulation area. The other valleys we studied likely received less wind drift: cirques in Ih Bogd and Sutai ranges are upwind (west) of a plateau that accumulates much snow. Thus, the additional accumulation of snow on Mönh Mösnii cirque due to local factors likely pushed across the threshold for glaciation, driving the glaciers to lower altitudes than expected from regional climatic conditions alone.

According to the calculation of Rupper and Roe (2008) of melt fractions (Fig. 3) melt becomes responsible for more than 50% of total ablation when annual precipitation is higher than ~150 mm, which marks the transition from melt-dominated to sublimation-dominated regimes. Precipitation in our five sites bracketed this threshold. At Sutai, Ih Bogd and the Hangai ranges, precipitation is

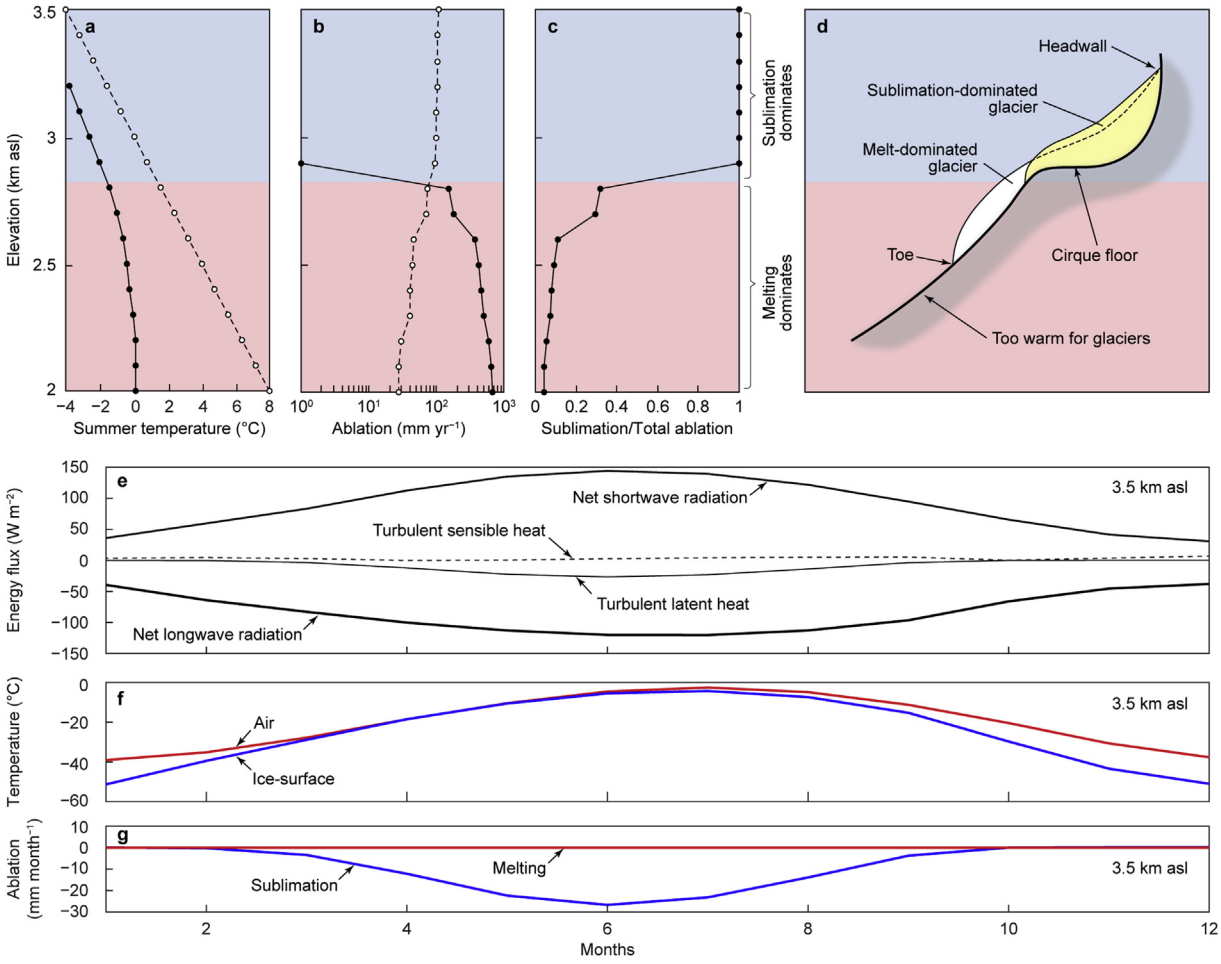

Fig. 11. Sublimation- and melt-dominated regime for glacier ablation. a. Summer (JJA average) air temperature (open circles) and ice-surface temperature (closed circles). b. Potential annual ablation from sublimation (open circles) and from melting (closed circles). Note the logarithmic scale for horizontal axis. c. Fraction of sublimation to total annual ablation. Sublimation dominates in "blue zone," where at least 50% of ice is lost via sublimation. The transition to the melt-dominated "red zone" is abrupt due to efficient melting. d. Profiles of two hypothetical glaciers under the same conditions except snowfall. The glacier with 110 mm (w.e.) yr^{-1} accumulation is balanced with sublimation before reaching the "red zone" below. An accumulation of 250 mm (w.e.) yr^{-1} will exceed sublimation and the glacier must flow to lower altitudes where melting occurs. e. Monthly mean calculations in the sublimation zone at 3500 m asl of incoming (positive) and outgoing (negative) energy fluxes: f. Monthly mean temperatures of air (top red line) and the ice-surface (bottom blue line); g. Monthly mean ablation due to melting (top red line) and sublimation (bottom blue line).

great enough that for glaciers to exist, efficient melting must dominate the total ablation, and the balance of T_a and snowfall controls the glaciation. The peaks of Otgontenger (4008 m asl) and Sutai (4220 m asl) have modern ice caps; yet the peak of Ih Bogd (3957 m asl, only ~140 m lower than the headwall of the modern Sutai glaciers) and with essentially the same climate, does not. The measured summer lapse rate at Sutai (8 °C km^{-1}; Online Supplement 1) applied to that altitude difference suggests that the Ih Bogd plateau could have a modern ice cap if it were at an altitude like Sutai or Otgontenger. At the Gichginii range, however, precipitation is so low that sublimation alone would be enough to ablate most of the snow and ice even if the summit plateau was higher and colder than Sutai or Otgontenger. Thus, the Gobi-Altai and southern Hangai ranges appear to be very close to the threshold of glaciation today. Evidently, as predicted by numerical models (Rupper and Roe, 2008; Rupper et al., 2009), in the arid environments of the Gobi-Altai insolation and summer T_a are important factors controlling ice mass balance, and minor variations in snowfall as well as T_a can lead to major changes in ELAs.

In considering precipitation-sensitive or sublimation-dominated glaciers, it is important to recognize that melting can also occur, just as some sublimation occurs in temperature-sensitive or melt-dominated systems. Some melting under cold conditions can occur even if $T_a \ll 0$ °C. This can occur at the thin edges of snow fields or glaciers, where sunlight can penetrate to a low-albedo substrate, warming it and melting the adjacent ice. It can also occur on glacier surfaces, especially if they are covered with a low-albedo layer of dust that can absorb the sunlight and warm the underlying ice. An example of the former is shown in Fig. 13, a photograph on the South Col of Chomolungma (Mt. Everest) at 8000 m asl and with $T_a \approx -28$ °C. It is noteworthy that blowing dust is common in Mongolia, and glaciers there may have been darkened accordingly, perhaps even more than they are today and in our energy modeling, which assumed "clean" ice.

4.2. Implications for reconstructing paleoclimate from glacier records

Without an actual measurement of glacier mass balance the ELA must be defined from the altitude of the highest lateral moraine, or from the geometry of the glacier using the THAR and AAR methods. These geometric ELAs are estimated from the altitudes of glacial deposits for paleoglaciers (e.g., Porter, 2001; Heyman, 2014) and using satellite images for modern glaciers (e.g., Kargel et al., 2014),

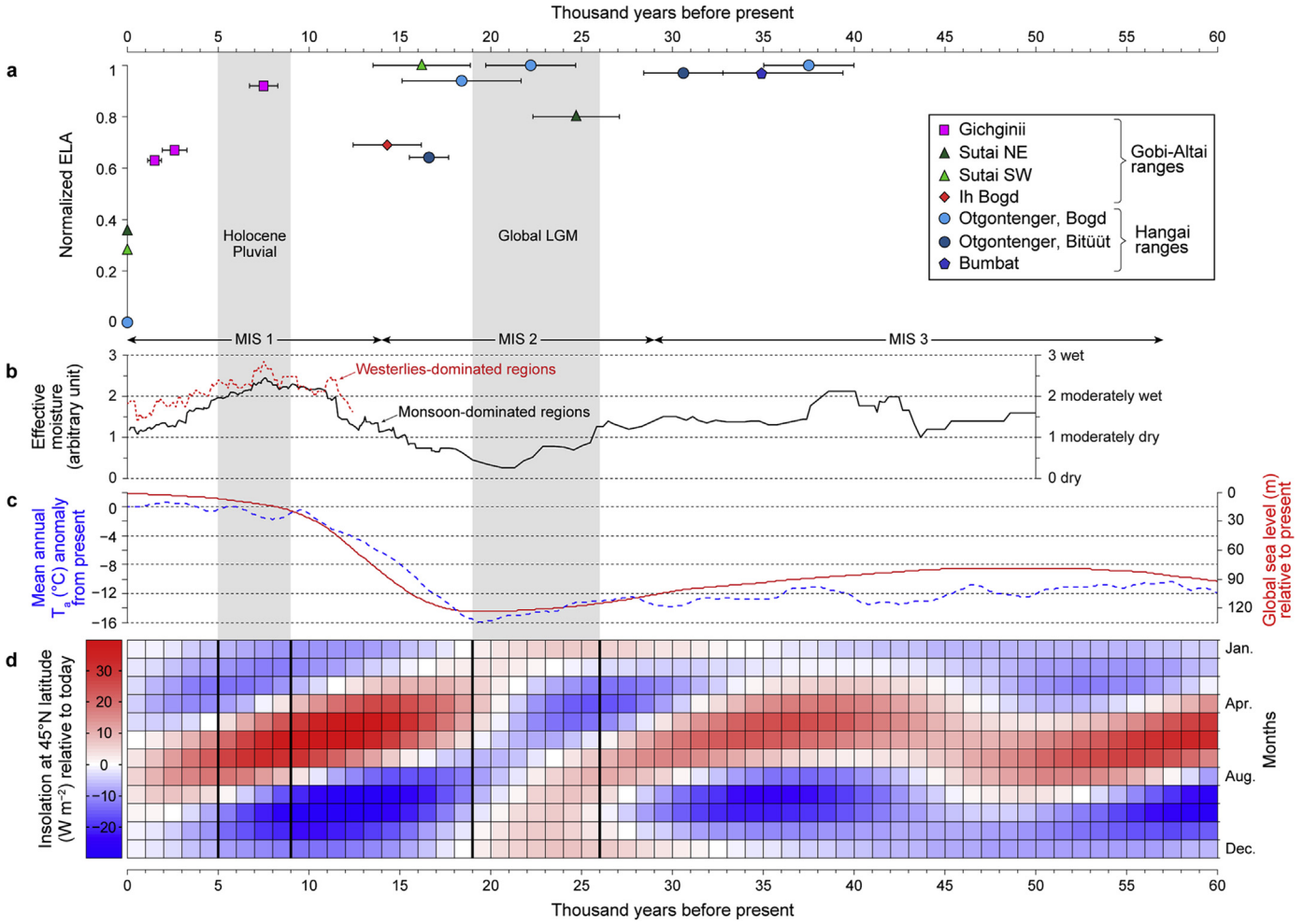

Fig. 12. Timing of local glaciation and the equilibrium-line altitude (ELA) lowering in the studied areas and the changes in regional climate. a. ELA depressions normalized to the ELA during the local LGM (Eqn (1)) and the corresponding mean moraine ages with 1σ total uncertainties shown as bracketed line. Dark green triangle for Sutai NE slope and light blue circle for Bogd river valley of Otgontenger are at zero because there are no glaciers today but the ice caps lie above the headwall. The Otgontenger data include ages from Rother et al. (2014) and this study. b. Average effective moisture (precipitation minus evaporation) reconstructed for regions dominated by westerlies (dashed red line) and monsoon (solid black line) in Central Asia (Herzschuh, 2006). The gray bars correspond to the durations of MIS 2 and the Holocene pluvial period in Mongolia. c. Mean annual surface air temperature for subarctic (40° N–80° N) continents (blue dashed line), and global sea level (red solid line), modeled from the LR-04 marine benthic oxygen isotope stack (Bintanja and van de Wal, 2008). d. Monthly insolation change from today at 45° N latitude.

Table 2
Average age and total uncertainty for ^{10}Be ages grouped according to landform. The groups are ordered from old to young.

Geographic region	Site	Group	n	Average age[a] (ka ± 1σ)	Interpreted deposition age[b] (ka)
Gobi-Altai	Gichginii	G2	3	7.5 ± 0.8	8–7
		G3	4	2.6 ± 0.7	3–2
		G4	6	1.5 ± 0.4	2–1
	Sutai	NE2-4	3	24.7 ± 2.4	27–22
		SW2	4	16.2 ± 2.7	19–13
	Ih Bogd	IB5-6	5	14.3 ± 1.9	16–12
Hangai	Otgontenger	BO1	3	22.2 ± 2.5	25–20
		BI2	2	30.6 ± 2.2	33–28
		BI9	2	16.6 ± 1.1	17–16
	Bumbat	BU1	3	59.9 ± 41.1	≫ 22 (?)
		BU2	4	34.9 ± 4.5	39–30

[a] Outliers are not included in averaging. The modified Kolmogorov-Smirnov test (Lilliefors,1967) of all the ^{10}Be ages, including the outliers, shows that the ages are normally distributed. Thus, the average age and the compounded uncertainty properly characterizes the timing of the moraine formation.
[b] Exposed boulders are the last ones to be deposited on a moraine when a glacier was advancing or was in standstill. Thus, the ^{10}Be boulder ages predate the retreating of the glacier.

and essentially make a metric with which to reconstruct climate from glacial advances and retreats. However, the physical ELA that is truly derived from physical glacier modeling requires a full account of surface energy and mass balance for individual glaciers.

Fig. 13. Ephemeral running water at the end of a snow field on the South Col of Chomolungma (Mt Everest) at 8000 m asl and $T_a \approx -28$ °C. Photograph by Justin Merle, 20 May 2009.

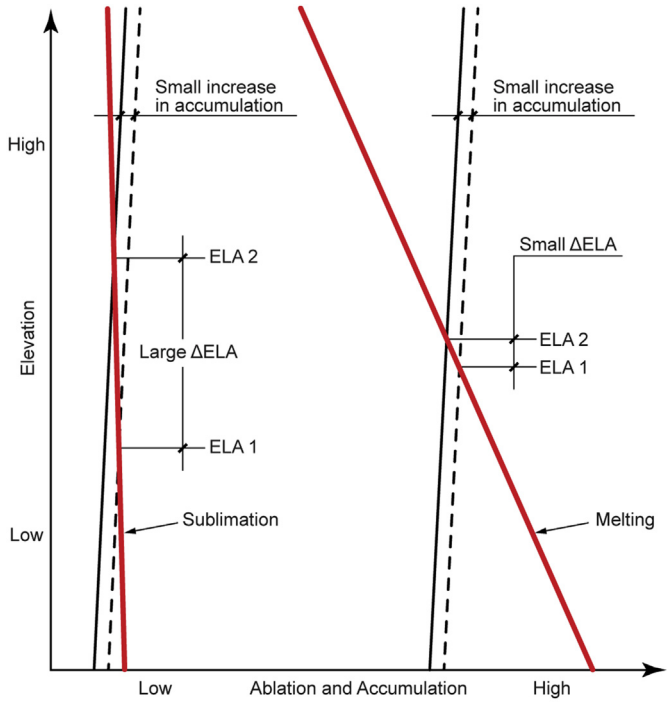

Fig. 14. Schematic diagram relating ELA depression (ΔELA) to change in precipitation. A small increase in precipitation (black line) shifts the amount towards right to the dashed line. In the sublimation-dominated glacier (Left) the ELA is sensitive to precipitation and a small increase in precipitation leads to large ΔELA. However, in melt-dominated glacier (Right) the ELA is insensitive to precipitation and the same increase in precipitation leads to much smaller ΔELA.

The correlation of geometric and physical ELAs for melt-dominated glaciers is well-defined (Ohmura et al., 1992), and because their ELA is a strong function of T_a (Fig. 10; Rupper and Roe, 2008) it is practical to reconstruct summer T_a from changes in ELA assuming minimal change in precipitation. However, the physical ELA for a sublimation-dominated glacier is poorly defined because no melting occurs and because the ablation in the higher "accumulation" zone is as strong as it is in the lower "ablation" zone. Moreover, sublimation (thus total ablation) is largely independent of T_a and small changes in precipitation can drive large changes in ELA (Fig. 14).

In the warming climate caused by human activities (IPCC, 2013) many glaciers are already retreating (Roe et al., 2016). Once limited to their cirques, some will be subject to the same kind of idiosyncratic local factors that we conclude have occurred in the past across the Gobi-Altai, making regional patterns of glacier balance more "noisy" and difficult to interpret in terms of climate. Mountain glaciers now in the "precipitation-sensitive" regime (blue dots of Fig. 10) may migrate towards the "temperature-sensitive" regime (red dots of Fig. 10) and in the absence of greatly increased winter snowfall they may retreat catastrophically. Still, other and colder glaciers in the "precipitation-sensitive" regime may simply lengthen as warmer conditions bring increased precipitation without causing them to cross into the "transitional" zone (black dots of Fig. 10) and/or "temperature-sensitive" regime. Thus, asynchronous behavior should be expected in the future, even under climate-change conditions of simple warming. Our analyses (Fig. 12) have suggested that under specific conditions some glaciers do not require a cooling climate to advance, and that glacier records can best be understood by identifying the major ablation processes dictating the glacier sensitivity to changes in climate, as predicted by numerical modeling of Rupper and Roe (2008).

5. Summary and conclusions

The paleoglaciers in Gichginii range of central Gobi-Altai, advanced at ~8–7 ka, during the early Holocene, with a magnitude similar to their local LGM positions. During the early Holocene, the autumn and spring were warmer than in the global LGM, but the resulting increased ice loss due to melting and sublimation was compensated by increased regional precipitation sufficient to cause a regional pluvial period of high lakes. Additional snow accumulation due to wind drift and shaded cirques also favored Holocene glacier growth. Although the timing of the local LGM at Gichginii was not constrained, for times prior to 10 ka in these cold, extremely arid environments evidently inefficient sublimation could ablate the meager amount of annually accumulated snow and ice, resulted in small glacier advances despite the low temperatures.

In contrast to the temporal pattern of maximum glaciations and arid climate in the Gichginii range, other mountain ranges with higher precipitation in the Gobi-Altai, for example in Artsan valley of Ih Bogd and the southwest slopes of Sutai, remained at least intermittently glaciated until ~16–14 ka, after the global LGM. The largest global LGM advance in the Gobi-Altai was observed on the northeast slopes of Sutai (ELA = 3640–3280 m asl; ΔELA = 260–590 m). In Bumbat valley, in the less arid Hangai ranges, the glaciers advanced to their maximum at ~40–30 ka, during MIS 3 and well before the global LGM. Melting dominates ablation in those subhumid areas and increased precipitation

during MIS 3 would have driven the glacier advance. However, the Hangai paleoglaciers 20 km west of the Otgontenger ice cap achieved their maximum extent at ~22 ka, during the global LGM. They were similar in size to those of MIS 3 (ELA = 2840–2670 m asl; ΔELA ≈ 1000 m), mainly because over the past 60 ka regional precipitation was at its lowest level during the global LGM even though there was a slightly lower average air temperature in MIS 2 than in MIS 3, which favored glacier growth.

There are three broad implications that can be drawn from our findings: 1) The notion of a near-synchronous northern-hemisphere LGM advances of mountain glaciers is not widely applicable to cold, sub-freezing arid regions; 2) Although less energy-efficient than melt, sublimation becomes more important and can even dominate ablation of glaciers in such regions, where glacier growth there is largely controlled by precipitation and is less sensitive to air temperature; 3) Under modern global climate warming, most glaciers are in retreat, but our results suggest that, although non-intuitively, in some regions, particularly cold deserts, the indirect result of warming could be glacial advance due to increased snowfall. Therefore, changes in glacier growth must be interpreted cautiously to infer climatic past and future conditions.

Acknowledgements

We are grateful to D. Sukhbaatar (Damdin-Da Fund) for logistical support and to R.M. Burke, D.H. Clark and Z.P. Lai for assistance in the field. We acknowledge J. Stone for help in preparing the samples, J. Levine for providing the codes for calculating insolation, and A. Sakai for providing the GAMDAM dataset. Field work and sample analysis were funded by the Don J Easterbrook Distinguished Scientist Award to A.R. Gillespie, a graduate research award to J. Batbaatar, from the Department of Earth and Space Sciences, UW, and funding from the Quaternary Research Center, UW. We thank J. Heyman and an anonymous reviewer for helpful comments, which improved the manuscript.

Appendix A. Supplementary data

Supplementary data related to this article can be found at https://doi.org/10.1016/j.quascirev.2017.12.001.

References

Aizen, E.M., Aizen, V.B., Takeuchi, N., Mayewski, P.A., Grigholm, B., Joswiak, D.R., Nikitin, S.A., Fujita, K., Nakawo, M., Zapf, A., Schwikowski, M., 2016. Abrupt and moderate climate changes in the mid-latitudes of Asia during the Holocene. J. Glaciol. 1–29. https://doi.org/10.1017/jog.2016.34.

Annan, J.D., Hargreaves, J.C., 2013. A new global reconstruction of temperature changes at the Last Glacial Maximum. Clim. Past. 9, 367–376.

Augustin, L., Barbante, C., Barnes, P.R.F., Barnola, J.M., Bigler, M., Castellano, E., Cattani, O., Chappellaz, J., Dahl-Jensen, D., Delmonte, B., Dreyfus, G., Durand, G., Falourd, S., Fischer, H., Flueckiger, J., Hansson, M.E., Huybrechts, P., Jugie, G., Johnsen, S.J., Jouzel, J., Kaufmann, P., Kipfstuhl, J., Lambert, F., Lipenkov, V.Y., Littot, G.C., Longinelli, A., Lorrain, R., Maggi, V., Masson-Delmotte, V., Miller, H., Mulvaney, R., Oerlemans, J., Oerter, H., Orombelli, G., Parrenin, F., Peel, D.A., Petit, J.-R., Raynaud, D., Ritz, C., Ruth, U., Schwander, J., Siegenthaler, U., Souchez, R., Stauffer, B., Steffensen, J.P., Stenni, B., Stocker, T.F., Tabacco, I.E., Udisti, R., van de Wal, R.S.W., van den Broeke, M., Weiss, J., Wilhelms, F., Winther, J.-G., Wolff, E.W., Zucchelli, M., 2004. Eight glacial cycles from an Antarctic ice core. Nature 429, 623–628.

Balco, G., Stone, J.O., Lifton, N.A., Dunai, T.J., 2008. A complete and easily accessible means of calculating surface exposure ages or erosion rates from ^{10}Be and ^{26}Al measurements. Quat. Geochronol. 3, 174–195.

Batbaatar, J., Gillespie, A.R., 2016. Outburst floods of the Maly Yenisei. Part II – new age constraints from Darhad basin. Int. Geol. Rev. 58, 1753–1779.

Benn, D.I., Owen, L.A., 1998. The role of the Indian summer monsoon and the mid-latitude westerlies in Himalayan glaciation: review and speculative discussion. J. Geol. Soc. 155, 353–363.

Bintanja, R., van de Wal, R.S.W., 2008. North American ice-sheet dynamics and the onset of 100,000-year glacial cycles. Nature 454, 869–872.

Blomdin, R., Stroeven, A.P., Harbor, J.M., Lifton, N.A., Heyman, J., Gribenski, N., Petrakov, D.A., Caffee, M.W., Ivanov, M.N., Hättestrand, C., Rogozhina, I., 2016. Evaluating the timing of former glacier expansions in the Tian Shan: a key step towards robust spatial correlations. Quat. Sci. Rev. 153, 78–96.

Braconnot, P., Otto-Bliesner, B., Harrison, S., Joussaume, S., Peterchmitt, J.Y., Abe-Ouchi, A., Crucifix, M., Driesschaert, E., Fichefet, Th, Hewitt, C.D., Kageyama, M., Kitoh, A., Laîné, A., Loutre, M.F., Marti, O., Merkel, U., Ramstein, G., Valdes, P., Weber, S.L., Yu, Y., Zhao, Y., 2007. Results of PMIP2 coupled simulations of the Mid-Holocene and Last Glacial Maximum – Part 1: experiments and large-scale features. Clim. Past. 3, 261–277.

Chauvenet, W., 1960, 1863 Reprint of 1891. A Manual of Spherical and Practical Astronomy, fifth ed., vol. II, pp. 473–566 Dover, N.Y.

Clark, P.U., Dyke, A.S., Shakun, J.D., Carlson, A.E., Clark, J., Wohlfarth, B., Mitrovica, J.X., Hostetler, S.W., McCabe, A.M., 2009. The last glacial maximum. Science 325, 710–713.

Cuffey, K.M., Paterson, W.S.B., 2010. The Physics of Glaciers, fourth ed. Elsevier, Amsterdam.

Darvill, C.M., Bentley, M.J., Stokes, C.R., Shulmeister, J., 2016. The timing and cause of glacial advances in the southern mid-latitudes during the last glacial cycle based on a synthesis of exposure ages from Patagonia and New Zealand. Quat. Sci. Rev. 149, 200–214.

Fink, D., Smith, A., 2007. An inter-comparison of ^{10}Be and ^{26}Al AMS reference standards and the ^{10}Be half-life. Nucl. Instr. Meth. Phys. Res. B 259, 600–609.

Gibbons, A.B., Megeath, J.D., Pierce, K.L., 1984. Probability of moraine survival in a succession of glacial advances. Geology 12, 327–330.

Gillespie, A.R., 1991. Testing a new climatic interpretation for the tahoe glaciation. California, Proceedings of the White Mountain Research Station. Symposium. In: Hall Jr., C.A., Doyle-Jones, V., Widawski, B. (Eds.), I Natural History of eastern California and High-Altitude Research, vol. 3. University of California, Los Angeles, pp. 383–398.

Gillespie, A., Molnar, P., 1995. Asynchronous maximum advances of mountain and continental glaciers. Rev. Geophys. 33, 311–364.

Gillespie, A.R., Burke, R.M., Komatsu, G., Bayasgalan, A., 2008. Late Pleistocene glaciers in Darhad basin, northern Mongolia. Quat. Res. 69, 169–187.

Goldthwait, R.P., 1970. Mountain glaciers of the residential range in New Hampshire. Arct. Antarct. Alp. Res. 2, 85–102.

Gribenski, N., Jansson, K., Lukas, S., Stroeven, A., Harbor, J., Blomdin, R., Ivanov, M., Heyman, J., Petrakov, D., Rudoy, A., Clifton, T., Lifton, N., Caffee, M., 2016. Complex patterns of glacier advances during the lateglacial in the chagan-uzun valley. Russian Altai. Quat. Sci. Rev. 149, 288–305. https://doi.org/10.1016/j.quascirev.2016.07.032.

Hays, J.D., Imbrie, J., Shackleton, N.J., 1976. Variations in the Earth's orbit: pacemaker of the ice ages. Science 194, 1121–1132.

Herzschuh, U., 2006. Palaeo-moisture evolution in monsoonal Central Asia during the last 50,000 years. Quat. Sci. Rev. 25, 163–178.

Heyman, J., Stroeven, A., Caffee, M.W., Hättestrand, C., Harbor, J.M., Li, Y., Alexanderson, H., Zhou, L., Hubbard, A., 2011a. Palaeoglaciology of bayan har shan, NE tibetan plateau: exposure ages reveal a missing LGM expansion. Quat. Sci. Rev. 30, 1988–2001.

Heyman, J., Stroeven, A.P., Harbor, J.M., Caffee, M.W., 2011b. Too young or too old: evaluating cosmogenic exposure dating based on an analysis of compiled boulder exposure ages. Earth Planet. Sci. Lett. 302, 71–80.

Heyman, J., 2014. Paleoglaciation of the Tibetan Plateau and surrounding mountains based on exposure ages and ELA depression estimates. Quat. Sci. Rev. 91, 30–41.

Hughes, P.D., Gibbard, P.L., Ehlers, J., 2013. Timing of glaciation during the last glacial cycle: evaluating the concept of a global 'Last Glacial Maximum' (LGM). Earth-Sci. Rev. 125, 171–198.

IPCC, 2013. In: Stocker, T.F., Qin, D., Plattner, G.K., Tignor, M.M., Allen, S.K., Boschung, J., Nauels, A., Xia, Y., Bex, V., Midgley, P.M. (Eds.), Climate Change 2013: the Physical Science Basis. Cambridge Univ. Press.

Jin, L., Chen, F., Morrill, C., Otto-Bliesner, B.L., Rosenbloom, N., 2012. Causes of early Holocene desertification in arid central Asia. Clim. Dyn. 38, 1577–1591.

Kalnay, E., Kanamitsu, M., Kistler, R., Collins, W., Deaven, D., Derber, J., Gandin, L., Saha, S., White, G., Woollen, J., Zhu, Y., Chelliah, M., Ebisuzaki, W., Higgins, W., Janowiak, J., Mo, K.C., Ropelewski, C., Wang, J., Leetma, A., Reynolds, R., Jenne, R., 1995. The NCEP/NCAR 40-year re-analysis project. Bull. Amer. Meteor. Soc. 77, 437–471.

Kargel, J.S., Leonard, G.J., Bishop, M.P., Kääb, A., Raup, B.H. (Eds.), 2014. Global Land Ice Measurements from Space. Springer Praxis, Berlin. https://doi.org/10.1007/978-3-540-79818-7.

Kohl, C.P., Nishiizumi, K., 1992. Chemical isolation of quartz for measurement of in-situ -produced cosmogenic nuclides. Geochim. Cosmochim. Acta 56, 3583–3587.

Koppes, M., Gillespie, A.R., Burke, R.M., Thompson, S.C., Stone, J., 2008. Late quaternary glaciation in the Kyrgyz tien shan. Quat. Sci. Rev. 27, 846–866.

Lal, D., 1991. Cosmic ray labeling of erosion surfaces: in situ nuclide production rates and erosion models. Earth Planet. Sci. Lett. 104, 424–439.

Lilliefors, H.W., 1967. On the Kolmogorov-Smirnov test for normality with mean and variance unknown. J. Am. Stat. Assoc. 62, 399–402.

Matthews, J.A., Briffa, K.R., 2005. The 'little ice age': Re-evaluation of an evolving concept. Geogr. Ann. A 87, 17–36.

Mayewski, P.A., Rohling, E.E., Stager, J.C., Karlen, W., Maasch, K.A., Meeker, L.D., Meyerson, E.A., Gasse, F., van Kreveld, S., Holmgren, K., Lee-Thorp, J., Rosqvist, G., Rack, F., Staubwasser, M., Schneider, R.R., Steig, E.J., 2004. Holocene climate variability. Quat. Res. 62, 243–255.

Miehe, G., Schültz, F., Miehe, S., Opgenoorth, L., Cermak, J., Samiya, R., Jäger, E.J.,

Wesche, K., 2007. Mountain forest islands and Holocene environmental changes in Central Asia: a case study from the southern Gobi Altay, Mongolia. Palaeogeogr. Palaeoclimatol. Palaeoecol. 250, 150–166.
Mitchell, T.D., Philip, D.J., 2005. An improved method of constructing a database of monthly climate observations and associated high resolution grids. Int. J. Climatol. 25, 693–712.
Mix, A.C., Bard, E., Schneider, R., 2001. Environmental processes of the ice age: land, oceans, glaciers (EPILOG). Quat. Sci.Rev. 20, 627–657.
National Aeronautics and Space Administration, 2015. Shuttle Radar Topography Mission V3 Global 1 Arc Second Dataset (SRTMGL1) accessed July 2016 using Reverb version 10.128.2.
National Oceanic and Atmospheric Administration (NOAA), 2016. Integrated surface database (ISD), station Tonhil USAF ID 442660. Accessed from. http://www.ncdc.noaa.gov/isd in. October 2016.
Nuimura, T., Sakai, A., Taniguchi, K., Nagai, H., Lamsal, D., Tsutaki, S., Kozawa, A., Hoshina, Y., Takenaka, S., Omiya, S., Tsunematsu, K., Tshering, P., Fujita, K., 2015. The GAMDAM glacier inventory: a quality-controlled inventory of Asian glaciers. Cryosphere 9, 849–864. https://doi.org/10.5194/tc-9-849-2015.
Ohmura, A., Kasser, P., Funk, M., 1992. Climate at the equilibrium line of glaciers. J. Glaciol. 38, 397–411.
Owen, L.A., Richards, B., Rhodes, E.J., Cunningham, W.D., Windley, B.F., Badamgarov, J., Dorjnamjaa, D., 1998. Relic permafrost structures in the Gobi of Mongolia: age and significance. J. Quat. Sci. 13, 539–547.
Porter, S.C., 2001. Snowline depression in the tropics during the last glaciation. Quat. Sci. Rev. 20, 1067–1091.
Putnam, A.E., Schaefer, J.M., Denton, G.H., Barrell, D.J.A., Birkel, S.D., Andersen, B.G., Kaplan, M.R., Finkel, R.C., Schwartz, R., Doughty, A.M., 2013. The last glacial maximum at 44°S documented by a ^{10}Be moraine chronology at lake ohau, southern alps of New Zealand. Quat. Sci. Rev. 62, 114–141.
Roe, G.H., Baker, M.B., Herla, F., 2016. Centennial glacier retreat as categorical evidence of regional climate change. Nat. Geosci. https://doi.org/10.1038/ngeo2863.
Ross, S.M., 2003. Peirce's criterion for the elimination of suspect experimental data. J. Eng. Technol. 20, 38–41.
Rother, H., Lehmkuhl, F., Fink, D., Nottebaum, V., 2014. Surface exposure dating reveals MIS-3 glacial maximum in the Khangai Mountains of Mongolia. Quat. Res. 82, 297–308.
Rother, H., Shulmeister, J., Fink, D., Alexander, D., Bell, D., 2015. Surface exposure chronology of the Waimakariri glacial sequence in the Southern Alps of New Zealand: implications for MIS-2 ice extent and LGM glacial mass balance. Earth Planet. Sci. Lett. 429, 69–81.
Rupper, S., Roe, G., 2008. Glacier changes and regional climate: a mass and energy balance approach. J. Clim. 21, 5384–5401.
Rupper, S., Roe, G., Gillespie, A., 2009. Spatial patterns of Holocene glacier advance and retreat in Central Asia. Quat. Res. 72, 337–346.
Rupper, S., Koppes, M., 2010. Spatial patterns in Central Asia climate and equilibrium line altitudes. In: IOP Conf. Series: Earth and Environmental Science, vol. 9, 012009. https://doi.org/10.1088/1755-1315/9/1/012009.
Sakai, A., Nuimura, T., Fujita, K., Takenaka, S., Nagai, H., Lamsal, D., 2015. Climate regime of asian glaciers revealed by GAMDAM glacier inventory. Cryosphere 9, 865–880. https://doi.org/10.5194/tc-9-865-2015.
Shi, Y., 2002. Characteristics of late quaternary monsoonal glaciation on the tibetan plateau and in east Asia. Quat. Int. 97–98, 79–91.
Schneider, U., Becker, A., Finger, P., Meyer-Christoffer, A., Rudolf, B., Ziese, M., 2016. GPCC Full Data Reanalysis Version 7.0: Monthly Land-surface Precipitation from Rain Gauges Built on GTS Based and Historic Data. Research Data Archive at the National Center for Atmospheric Research, Computational and Information Systems Laboratory. Accessed January 2016. https://doi.org/10.5065/D6000072.
Stone, J.O., 2000. Air pressure and cosmogenic isotope production. J. Geophys. Res.–Sol. Ea. 105, 23753–23759.
Zomer, R.J., Trabucco, A., Bossio, D.A., Verchot, L.V., 2008. Climate change mitigation: a spatial analysis of global land suitability for clean development mechanism afforestation and reforestation. Agric. Ecosyst. Environ. 126, 67–80.